

Energy and angular momentum sharing in dissipative collisions

G. Casini¹, M. Bini¹, S. Calamai¹, R. Laforest^{2a}, P.R. Maurenzig¹, A. Olmi¹, G. Pasquali¹, S. Piantelli¹, G. Poggi¹, F. Saint-Laurent^{3b}, J.C. Steckmeyer², A.A. Stefanini¹, and N. Taccetti¹

¹ Istituto Nazionale di Fisica Nucleare and Università di Firenze, I-50125 Florence, Italy

² Laboratoire de Physique Corpusculaire, IN2P3-CNRS, ISMRA et Université, F-14050 Caen-Cedex, France

³ GANIL, DSM-CEA/IN2P3-CNRS, BP 5027, 14076 Caen-Cedex 5, France

Received: April 26, 2024/ Revised version:

Abstract. Primary and secondary masses of heavy reaction products have been deduced from kinematics and E-ToF measurements, respectively, for the direct and reverse collisions of ^{93}Nb and ^{116}Sn at 25 AMeV. Light charged particles have also been measured in coincidence with the heavy fragments. Direct experimental evidence of the correlation of energy-sharing with net mass transfer has been found using the information from both the heavy fragments and the light charged particles. The ratio of Hydrogen and Helium multiplicities points to a further correlation of angular momentum sharing with net mass transfer.

PACS. 25.70.Lm Strongly damped collisions, 25.70.Pq Multifragment emission and correlations

1 Introduction

It is now experimentally established that binary dissipative processes dominate the heavy-ion reaction cross-section also at intermediate bombarding energies (the so-called “Fermi” energies) up to about 50 AMeV [1,2,3,4,5,6]. This evidence, based on the results of experiments employing very different detectors and analysis methods, has stirred renewed interest on the subject of dissipative phenomena and calls for a deeper comprehension of the microscopic mechanisms capable of converting such large amounts of kinetic energy into excitation energy. The interest is increased by the fact that at intermediate energies dissipative processes, resembling in several aspects those known at low energies, coexist with new phenomena strictly related to the dynamics of the collision, so that the production of exotic and far from equilibrium pieces of nuclear matter may be expected.

In this context, strongly debated topics are, among others, pre-equilibrium and/or mid-rapidity emission of light particles, the possible formation and rupture of a hot neck as a source of intermediate mass fragments (IMF), the maximum amount of thermal energy which can be deposited in nuclei, the transfer of angular momentum from the entrance channel in the rotational modes of the fragments, the possible population of “doorway states” for nuclear vaporization. Another interesting and open field of investigation concerns the energy and angular momentum partition between the reaction partners of dissipative

collisions. This issue has been extensively debated in recent investigations [3,4,7,8,9], but it still remains to be convincingly clarified.

In previous works [9,10,11] we investigated heavy-ion reactions at bombarding energies from 10 to 24 AMeV, with special effort devoted to put into evidence, in a model-independent way, non-equilibrium effects in dissipative collisions. In a first paper [11], we studied the degree of equilibration between the two reaction partners at the end of the interaction phase employing the sequential fission channel. We measured fission probabilities of the fragments produced in an asymmetric reaction ($^{120}\text{Sn} + ^{100}\text{Mo}$ at 19.1 AMeV) where a given primary mass A corresponds to different net mass transfers for projectile- and target-like fragments (PLF and TLF). The main result was that the curves of fission probability P_{fiss} vs. fissioning mass A for PLF and TLF do not coincide. For a given A intermediate between target and projectile, P_{fiss} for the TLF (which gained mass) was significantly larger than for the PLF, even at large TKEL (Total Kinetic Energy Loss). The observed effect is a clear signature of the lack of an overall equilibrium at the end of the interaction.

More recently, we refined a method previously suggested by other authors [12], thus obtaining a model independent information on the partition of dissipated energy [9]. The most interesting result of our work (concerning the collision $^{100}\text{Mo} + ^{120}\text{Sn}$ at 14.1 AMeV), was the observation of a sharp correlation between the number of evaporated nucleons and the net exchanged mass for PLF and TLF, which we interpreted as an evidence for non-equilibrium excitation energy partition between the reaction products. This kind of correlation had been found and widely debated in previous works [12,13,14,15,

^a *Permanent Address:* Washington University, Medical School, BOX 8225 510 Kingshiway, St-Louis, MO 63110

^b *Permanent Address:* DRFC/STEP, CEA/Cadarache, F-13108 Saint-Paul-lez-Durance Cedex, France

16] but clear conclusions on its strength and implications have not yet been drawn.

Here we want to briefly summarize the terms of the debate on this subject. At rather low bombarding energies (8-15 AMeV) [15, 17, 18, 19], several experimental findings (concerning mass and charge drift, mass and charge variances, excitation energies of reaction products) can be qualitatively understood in the frame of the nucleon exchange model (NEM) [20, 21]. In some cases a quantitative agreement can be obtained, although the experimental variances tend to be systematically underestimated. The NEM assumes that energy dissipation takes place via a number of stochastic exchanges of single nucleons between the two fragments when they are in contact along the trajectory. At the beginning of the interaction, the NEM predicts that the cold nuclei gain almost the same amount of energy due to the random nature of the exchanges; as a consequence a thermal non-equilibrium develops which increases with increasing mass-asymmetry of the interacting nuclei. This thermal disparity tends to be smoothly reduced by the following nucleon transfers which force the dinuclear system to recover thermal equilibrium. As a consequence, if the duration of the contact is long enough (as it happens at lower impact parameters and at lower bombarding energies), the statistical decay of the two outgoing fragments should be consistent with the same value of the temperature (which corresponds to an energy partition proportional to the primary mass of the final fragments).

Indeed, such a behavior has been found in many works [8, 12, 14, 15, 17, 18, 19, 22, 23, 24, 25, 26] which were aimed at studying the average excitation energy sharing in heavy-ion collisions as a function of the dissipation, commonly estimated by the total kinetic energy loss (TKEL); the word “average” means here that the data are integrated, for each TKEL bin, over the mass distribution of the primary excited fragments. In these works, with increasing dissipation, a trend towards equilibrium partition (*i.e.*, excitation energy shared in proportion to the mass of the fragments) is observed; however, this condition seems to be never reached [19, 23, 24, 26].

More refined experiments [9, 12, 13, 14, 15] have claimed that the excitation energy division is correlated with the net mass transfer, with an excess of excitation being deposited in the fragment which gains nucleons. By itself, the existence of such a correlation is compatible with the NEM framework. In fact, especially for trajectories leading to rather peripheral collisions, it is likely that most of the excitation produced in each exchange comes from the damping of the fairly high relative velocity of the transferred nucleon in the almost cold receptor nucleus. Thus, reaction products have necessarily more excitation energy when they have experienced mass gain than in the opposite case when they have finally lost nucleons. However, the observation that this correlation seems to be largely independent of the degree of inelasticity [9, 15] is another feature difficult to understand within the present version of the stochastic nucleon exchange model and deserves new investigation. In order to clarify this aspect of dis-

sipative collisions we have studied the collision $^{93}\text{Nb} + ^{116}\text{Sn}$ at 24.9 AMeV.

The paper is structured as follows. In sect. 2 a description of the detector array and of the experimental methods is given. Section 3 shows the experimental results which are divided in two parts. The first one concerns data on total mass evaporated from the PLF as a function of its primary mass A and TKEL (sect. 3.1); the second part deals with light charged particles emitted from PLF and directly detected with an array of plastic scintillators (sect. 3.2). Particular care is devoted to describe the possible biases introduced by the measurement and analysis methods and the way in which they have been taken into account and corrected for employing Monte Carlo calculations. Details on this latter subject can be found in the Appendix. Finally, sect. 4 presents a discussion of the results, partly based on a comparison with statistical model calculations performed with the code GEMINI [27].

2 Experimental set-up and methods

2.1 The measurement

Beams of ^{93}Nb and ^{116}Sn at 24.9 AMeV were delivered by the GANIL accelerator, with an excellent time resolution of about 550 ps (FWHM) for Nb and 350 ps (FWHM) for Sn. They were used to study the slightly asymmetric system $^{116}\text{Sn} + ^{93}\text{Nb}$, both in direct and reverse kinematics, a method already applied in a previous experiment at lower bombarding energy [9]. The moderate asymmetry of the entrance channel was necessary in order to ensure a common range of masses for PLF and TLF even at moderate TKEL.

The choice of elements Nb and Sn was motivated by beam and target feasibility reasons, with the additional constraint of studying a system not too far from $^{100}\text{Mo} + ^{120}\text{Sn}$, previously studied at 14 AMeV at GSI [9]. The particular isotope of Sn was thus a compromise between the technical need for a sufficiently large natural abundance (to make it usable as a beam source) and the requirement of having an N/Z ratio (1.32) similar to that of ^{93}Nb (1.27), in order to reduce the possible role of isospin equilibration. Both targets consisted of foils of ^{93}Nb and isotopically enriched ^{116}Sn , with a thickness of about 200 $\mu\text{g}/\text{cm}^2$.

During most runs, the target was in a tilted position, with the beam impinging on it at an angle of about 45°. This choice, while not appreciably affecting the measurement of the fast forward-going PLF, was of utmost importance for a good measurement of the coincident TLF, especially for the slow ones emitted close to 90° (as in case of events with moderate energy dissipation). In this way one strongly reduces the average thickness of target material passed through by the TLF, drastically decreasing the perturbation of its velocity vector due to energy- and angle-straggling.

Shorter runs with other targets were also performed at the same bombarding energy. In particular, as it will be explained in the following, the data collected for the

two symmetric systems $^{116}\text{Sn}+^{116}\text{Sn}$ and $^{93}\text{Nb}+^{93}\text{Nb}$ were used for checks and corrections. Further information was obtained from short runs with the strongly asymmetric systems $^{116}\text{Sn}+^{58}\text{Ni}$ and $^{116}\text{Sn}+^{197}\text{Au}$ at the same energy.

Finally, for calibration purposes, data were recorded also for the system $^{93}\text{Nb}+^{93}\text{Nb}$ at a bombarding energy as low as 3.86 AMeV, obtained by switching off the second cyclotron of GANIL. In this way the whole set-up was illuminated with elastic scattering events.

2.2 The set-up

The experiment is based on the determination, as a function of TKEL, of the total mass evaporated from excited PLF, as given by the difference between their primary mass (obtained, via the kinematic coincidence method, from the velocity vectors measured by gas detectors) and secondary mass (via additional measurement of the kinetic energy by means of Silicon detectors). Additional information on the dissipative collisions was also obtained from the direct measurement of the light charged particles by means of scintillation detectors.

2.2.1 The gas detectors

An array of 12 large-area position-sensitive parallel-plate avalanche detectors (PPAD) was mounted inside the Nautilus scattering chamber. The detectors were arranged on three planes of four detectors each, in an almost axially symmetric geometry around the beam direction (see fig. 1 of ref. [1]). With respect to previous experiments at lower bombarding energies [1,10], the most forward plane was moved at a larger distance from the target (about 250 cm), in order to increase the flight-path, and the resulting larger dead-region between the forward and the middle plane was partially reduced by shifting two of the middle plane detectors toward the beam axis. Thus, in this experiment, the 12 gas detectors (each with an active area of $300\times 300\text{ mm}^2$) covered about 65% of the forward hemisphere.

The PPAD detected heavy ($Z\gtrsim 10$) reaction products, with about 100% intrinsic efficiency. They measured both the position of impact and the time-of-flight (with respect to the bunched beam) of the reaction products, thus yielding their velocity vectors. The position resolution of the PPAD was about 3.5 mm (FWHM) and the overall time-of-flight resolution (including the contribution of the beam) about 750 and 600 ps (FWHM) for the runs with Nb and Sn beam, respectively.

In the experiment, the most critical operating conditions were those of the most forward PPAD, due to the high counting rate of elastic and quasi-elastic products. Thus, typical beam currents of 0.1–0.5 nA (with charge states 31^+ and 37^+ for the two beams) were used to limit the maximum counting rate of the forward detectors to about $15\text{--}20\cdot 10^3$ counts/s. Moreover, in order to reduce the load on all detectors due to the flux of electrons extracted by the beam while passing through the target, a

positive high voltage of 40–42 kV was applied to the electrically insulated target holder. More details on the gas detectors can be found in [1].

2.2.2 The silicon detectors

Two identical arrays of 23 ion-implanted Silicon detectors each were mounted behind two of the four most forward PPAD. The Silicon detectors covered laboratory polar angles ranging from about 2° to about 7° , so that most of them were located below or around the grazing angles for the studied reactions, which vary from about 3.5° for the $^{116}\text{Sn}+^{58}\text{Ni}$ system to about 8.6° for the $^{116}\text{Sn}+^{197}\text{Au}$ one. The first 18 Silicon detectors of each array (manufactured by Eurisys Mesures) had an active area of about $30\times 30\text{ mm}^2$ and a thickness of about $500\mu\text{m}$, sufficient to fully stop the quasi-elastic PLF at these bombarding energies. They covered the region at smaller angles, approximately between 2° and 5.5° . In each array, larger angles up to about 7° were covered by 5 Silicon detectors (purchased from Micron Semiconductors for previous experiments) with an active area of $50\times 50\text{ mm}^2$ and a thickness of $300\mu\text{m}$. In order to fully stop quasi-elastic PLF, they were mounted in a tilted position with respect to the direction of the incoming particles, so that their effective thickness was increased to about $420\mu\text{m}$ and their effective area correspondingly reduced to about $35\times 50\text{ mm}^2$.

2.2.3 The scintillation detectors

For the measurement of the light charged particles (LCP) we took advantage of the scintillator array “Le Mur”, mounted at small angles on the closing cup of the NAUTILUS scattering chamber, behind the gas and Silicon detectors. This device consists of 96 pads of fast plastic scintillator NE102, 2 mm thick, mounted in 7 circular rings centered on the beam axis, with a threshold of about 3.2 AMeV for protons and α -particles. A detailed description of the geometry and performance of this device can be found in [28]. “Le Mur” allows a clean Z-identification of fast light reaction products punching through the thin scintillator material. For protons and α -particles this happens for energies greater than ≈ 13.5 AMeV.

Due to the primary need to optimize the time of flight resolution, the target holder had to be installed at one extreme of the scattering chamber, thus increasing the flight-path but significantly reducing the angular acceptance of the wall (polar angles from about 2° to about 18.5°). Moreover, the presence of our apparatus between target and “Le Mur” (with absorbing materials like detector frames, cables and supporting structure) produced large and complicated shadows on several plastic pads. In the analysis of the data it was then necessary to select a subset of pads which were reasonably clean and free from shadows. A first selection then was operated by cutting away all the pads in which distortions or anomalous lack of yield in the ridges for $Z=1$ and $Z=2$ particles were a clear evidence of shadowing. Some detectors of the inner

rings which were contaminated by the scattering of beam particles on the last collimator, as well as detectors in which poor resolution did not allow a clean separation of $Z=1$ and $Z=2$ particles, were discarded too. Finally, only 33 out of the original 96 pads were retained in the analysis. In the identification matrices also fast light fragments, such as Lithium or Beryllium, were visible above the ridges of $Z=1$ and $Z=2$ particles, however the cumulated statistics was low and they will not be considered in the present work.

The geometric acceptance of “Le Mur” was such that, for our slightly asymmetric systems, most of the detected LCP originate from PLF decay, except for very central collisions. We even strengthened this geometric selection by cutting away in the analysis all slow particles stopped in the pads, the amount of rejected particles being about 15–20% of the total.

2.3 Calibration and correction procedures

2.3.1 Kinematic coincidence method

A refined version of the kinematic coincidence method (KCM) [29] was applied and from the velocity vectors measured by the PPAD primary (pre-evaporative) quantities –in particular the masses of the heavy fragments and TKEL– were deduced event-by-event. Although this analysis can be applied to events with 2, 3 or 4 heavy fragments in the exit channel, the main interest of this work is concentrated on the binary channel. Therefore, unless otherwise explicitly stated, in the following we will refer only to measured binary events in which two heavy fragments (with charge $Z \gtrsim 10$) were detected by two PPAD and one of them was also stopped in one Silicon detector.

This version of the kinematic coincidence method allows to exploit the two-fold redundancy of the available experimental information for 2-body events. Indeed, it is based on the minimization of $\sum_{i=1,2} m_i^2 |(\mathbf{v}_i^{\text{exp}} - \mathbf{v}_i)|^2$ under constraint of mass and momentum conservation. It gives not only the best estimates of the unknown primary masses m_i , but also optimized “improved values” \mathbf{v}_i of the measured velocity vectors $\mathbf{v}_i^{\text{exp}}$, such that the conservation laws are exactly satisfied event-by-event. On the basis of statistical arguments [29], for binary events the distribution of the minimized quantity Δ_{KCM} is expected to be approximately shaped like a χ -distribution with 2 degrees of freedom. The width of the distribution increases with increasing perturbation of the 2-body kinematics (*i.e.*, with increasing dissipation).

2.3.2 Correction for misalignment of the set-up

A precise knowledge of the position of the detectors with respect to beam direction is mandatory for a kinematic reconstruction, especially in case of strongly forward-peaked kinematics. Therefore special care was devoted to the measurement of the geometry of the set-up and to its alignment along the nominal beam direction. The geometry of

the detectors was measured optically by means of a surveying instrument (Total Station) mounted in the target position. The nominal accuracy of the instrument for angle and distance measurements (the last one obtained via an infrared distantiometer and corner cubes on the detectors) is about 5” and ± 2 mm, respectively. Due to the uncertainty (± 0.5 mm) in the positioning of the instrument with respect to the target center and of the corner cubes with respect to the detectors, angular accuracies of the order of 6’ for the detectors closer to the target and of 40’ for the more distant ones are estimated. The absolute distance accuracy is the nominal one of ± 2 mm.

The beam was neatly focused onto the target center with the help of an alumina (Al_2O_3) plate mounted on the target ladder: the beam was steered until its luminescent spot almost disappeared into a hole (of 2 mm radius) drilled in the center of the alumina. The coincidence of actual direction of the beam with the one optically determined during the assembly of the setup was checked at run-time by a beam profiler (consisting of a small removable grid-detector) located on the beam axis about 3 m downstream of the target.

In the off-line analysis, the position of the detectors was checked with the data of elastic scattering of ^{93}Nb projectiles on light targets (^{12}C , ^{27}Al and ^{55}Mn), taken at the lower bombarding energy of 3.86 AMeV. In fact, in asymmetric systems and reverse kinematics, the elastic scattering of heavy projectiles presents a limiting angle, which in our case was $\theta_{\text{lab}}^{\text{limit}} \approx 7.4^\circ$, 16.9° and 36.3° for the three light targets, respectively. The presence of a limiting angle produces a circular ridge in the cross section $d^2\sigma/d\theta_{\text{lab}} d\phi$, characterized by a sharp drop of the intensity towards larger laboratory angles, thus allowing an easy consistency check of the geometry of the detectors.

Finally, the actual alignment of the beam axis with respect to the optical axis was checked in the off-line analysis by means of the elastically scattered projectiles which partially irradiated the four most forward PPAD in all studied reactions. To do so, it was assumed that the beam hits the target center, but its direction may present a slight deviation from the optical axis. The proper correction would then consist in a small rotation of the reference frame around the target center.

For each run, the angular distributions of elastically scattered projectiles hitting the four most forward PPAD (in clean equal windows of the azimuthal angle ϕ) were simultaneously fitted with the Rutherford cross section, $\sigma_{\text{Ruth}}(\theta_{\text{lab}})$. The “best” correction was determined by χ^2 minimization with respect to the applied reference frame rotation. For all runs, such a correction amounted to 0.1° at most (less than 4 mm in the plane of the most forward detectors).

2.3.3 Correction for pulse height defect

The Silicon detectors measured the kinetic energy of heavy fragments passing through the PPAD. From this kinetic energy, and from the time-of-flight (ToF) of the PPAD,

secondary masses for PLF were deduced employing an iterative procedure which includes corrections both for the “pulse height defect” (*PHD*) in Silicon and for the energy lost in the PPAD and in the dead layers of the Silicon chip. Quantitatively, both corrections represent a small fraction of the total kinetic energy for most ions. As an example, for elastically scattered ^{116}Sn or ^{93}Nb ions at 25 AMeV, the total energy-loss before reaching the active region of the Silicon chip amounts to about 1% of their energy, and the correction for the *PHD* in the bulk of the chip is at most comparable. However, since good accuracy in the energy measurement was a strong need for our analysis purposes, special effort has been devoted, both during the measurement and in the off-line analysis, to obtain a precise evaluation of the energy released in the Silicon detectors. Experimental values of *PHD* (extracted from data) were taken into account in the calibration and analysis. For a careful discussion of these aspects we refer to the technical paper [30]. Here, we only recall that the overall accuracy of the energy calibration is estimated to be around 0.5%.

In order to judge about the quality of the measurement of both primary and secondary mass of PLF, some experimental results are shown in fig. 1. Part a) presents the kinetic energy spectrum of PLF, measured with one of the Silicon detectors (located at $\approx 2.7^\circ$) in binary events of the $^{116}\text{Sn}+^{93}\text{Nb}$ reaction at 25 AMeV. One can clearly see the elastic peak, with a resolution of 7-8 MeV (FWHM), which represents a typical value for all the Silicon detectors. Gating on this peak (for each Silicon detector) gives an easy way to select (or exclude) elastic events in the analysis.

2.3.4 Corrections for position-dependent time-of-flight

Figures 1b,c,d show the resolutions in time-of-flight, primary and secondary mass, respectively, for elastic events selected by gating on the elastic peaks in the Silicon energy spectra. Here and in the following, the time-of-flights measured by the PPAD have been corrected for the dependence of signal propagation time on the position of impact on the PPAD. This correction was indeed crucial for obtaining the displayed good resolutions and was deduced, for all PPAD, from the analysis of pure elastic events produced in collisions at low bombarding energy ($^{93}\text{Nb}+^{93}\text{Nb}$ at 3.86 AMeV).

Figure 1b presents the distribution of the differences between the experimental time-of-flight of the PPAD and the one calculated via elastic scattering kinematics from the deflection angle measured by the PPAD. All events with projectiles hitting any one of the Silicon detectors behind one of the forward PPAD have been added. As can be seen, the overall time-of-flight resolution was indeed very good ($\Delta t \leq 600$ ps FWHM), thanks also to the high quality of the beam buckets delivered by the GANIL staff.

The primary mass distribution for these elastic events, as obtained from the kinematic coincidence method, is shown in fig. 1c. It is worth noting that the good mass resolution of about 2 amu (FWHM) depends also on the good

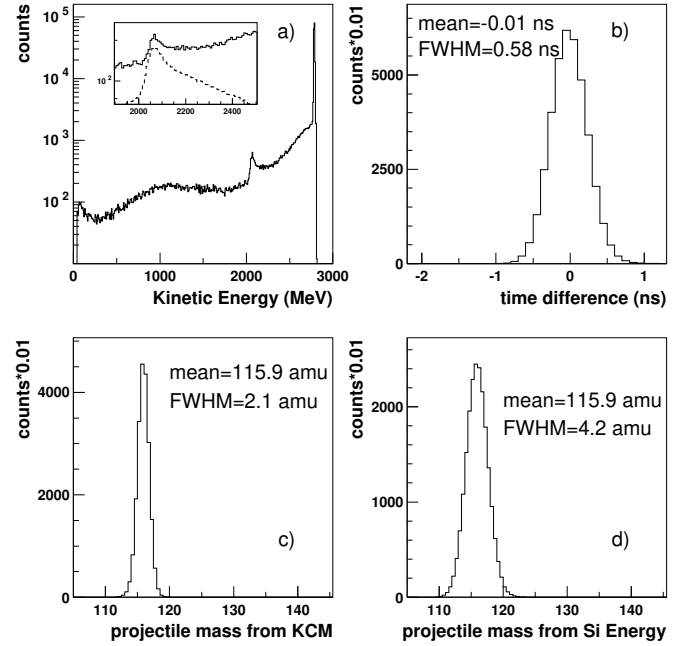


Fig. 1. a): Experimental kinetic energy spectrum measured with one of the Silicon detectors for binary events in the $^{116}\text{Sn}+^{93}\text{Nb}$ system at 25 AMeV. In this figure no subtraction of the ions scattered on the grid wires of the PPAD has been performed. In the portion of spectrum displayed in the inset, the continuous line represents all the 2-body events, while the dashed line is the estimated background due to the ions which pass through the grid wires of the PPAD before reaching the Silicon detector (see sect. 2.3.5 in the text). The data presented in the remaining panels of the figure have been gated by windows on the elastic peaks of the detectors. b): Distribution of the differences between measured and calculated time-of-flight for elastically scattered projectiles; all the Silicon detectors behind one of the PPAD were taken into account. c): Primary mass distribution of elastically scattered projectiles, obtained from binary events by means of the kinematic coincidence method. d): Secondary mass distribution obtained from the energy measured in the Silicon detectors and time-of-flight measured with the PPAD.

angular resolution for the very slow target recoil accompanying the fast projectile in these binary events. Finally, for the same sample of elastic events as in parts b) and c), fig. 1d shows the secondary mass distribution, which is obtained from quantities related solely to the PLF detection. As expected, in this case the mass resolution is dominated by the time-of-flight resolution which accounts for nearly 90% of the measured value of 4.2 amu (FWHM).

2.3.5 Effects of the wires of the gas detectors on PLF energy measurement

A tricky effect is connected with the measurement of the secondary mass of ions passing through the position sensitive PPAD. The grids of wires of the PPAD anodes, from

which the impact position is deduced, represent an inhomogeneous dead-layer for the impinging ions. At these high beam energies, energetic reaction products are not stopped in the wires, even not when they cross the whole diameter. In this case, one obtains the correct information on ToF and position from the PPAD, but the measured kinetic energy in the Silicon detectors is strongly degraded. This effect concerns a small fraction of events, about 4%, determined by the geometric “cross section” of the two orthogonal grids (each made of 20 μm diameter wires with a pitch of 1 mm). Due to the large intensity of the Rutherford cross section, a large amount of these kind of events corresponds to degraded elastically scattered projectiles, simulating inelastic events. They are responsible for the peaked distribution slightly above 2 GeV which can be clearly seen in fig. 1a.

However, not only the energy of the elastic projectiles, but also that of other inelastic products gets similarly degraded when passing through the PPAD, thus producing an unknown background of bad events, which one would like to single out and reject. Every attempt to eliminate them on the basis of correlations between measured quantities (like *e.g.* ToF and ΔE from PPAD and E from the Silicon detectors) introduced spurious cuts as a side-effect. Thus we devised an analysis procedure to get an average estimate of such a background. All reaction products detected in the Silicon detectors (including the elastic ones), were “passed” through a “simulated” grid, namely the point of impact on the wire was randomly chosen, the thickness of material calculated and the energy accordingly degraded (also the occurrence of double impacts on both grids was taken into account with the proper weight). The obtained “degraded” data were re-analyzed and the so estimated background was subtracted from all results based on the information of the Silicon detectors, with a suitable normalization chosen so as to remove the spurious peak in the energy spectra of fig. 1a.

The quality of the correction can be judged from the inset in fig. 1a, which shows a part of the kinetic energy spectrum. The continuous line represents all the 2-body events, while the dashed line represents the background of nuclei slowed down by the wire grids of the PPAD, as estimated with the above described procedure. Similar results are obtained for other detectors and for the $^{93}\text{Nb}+^{116}\text{Sn}$ reaction.

2.3.6 Calibration of the scintillators

An example of the correlation light-output vs. time-of-flight is presented in fig. 2 for the reaction $^{116}\text{Sn} + ^{93}\text{Nb}$ at 25 AMeV. In this correlation each species of light charged particles gives origin to a ridge divided into two branches by a cusp. To the left of the cusp there are fast particles punching through the thin scintillator, while to the right there are slower particles which are stopped in the material. The position of the cusp was used as a calibration point for the time-of-flight scale. In case of punching through particles, the light output is related to the energy lost in the material and a clean Z-identification

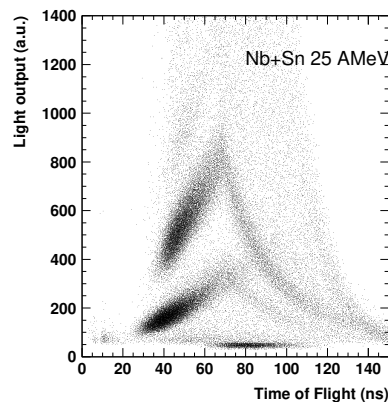


Fig. 2. Experimental scatter-plot of light-output vs. ToF for light charged particles measured with one of the pads of the scintillator array “Le Mur” for the system $^{93}\text{Nb}+^{116}\text{Sn}$ at 25 AMeV. The particles are detected in coincidence with two heavy reaction products in the PPAD. The ridges of energetic punching-through $Z=1$ and $Z=2$ particles are clearly visible.

can be achieved, in spite of quenching effects. The two intense branches on the left of fig. 2 correspond to energetic $Z=1$ and $Z=2$ particles. In case of stopped particles, the light output is related to their total energy, but strong quenching effects prevent a clean mass-identification. For example, it is well known that stopped α -particles become mixed up with stopped deuterons and tritons.

2.3.7 Background of incompletely detected events

As stated before, in this paper we focus on dissipative binary events, in which two heavy fragments were detected by the PPAD and one of them (usually the PLF) was also stopped in one of the Silicon chips. Similarly to previous works [1], also in the present case true binary events still represent a major part of the total reaction cross section (see sect. 3.1.1). However, a sizeable amount of higher multiplicity events is also produced, especially at high TKEL values. Therefore, because of the incomplete geometric coverage of the set-up, a certain fraction of the detected 2-body events are not true binary events, but rather partially detected events of multiplicity greater than two (mainly 3-body events). Following a procedure described in detail elsewhere [29], we estimated and subtracted this background from the data.

The continuous histograms in fig. 3 show, for some bins of Total Kinetic Energy (TKE) in the reaction $^{93}\text{Nb} + ^{116}\text{Sn}$ at 25 AMeV, the experimental distributions of Δ_{Kcm} , the quantity minimized in the kinematic coincidence analysis. It has been verified that the histograms are approximately shaped like a χ -distribution with 2 degrees of freedom [29], except for the long flat tails. The dotted histograms give the (estimated) 3-body background obtained by analyzing the measured 3-body events (with one fragment in one Silicon detector) as if they were binary events, after having randomly removed one of the two fragments which did not hit the Silicon detector. They have

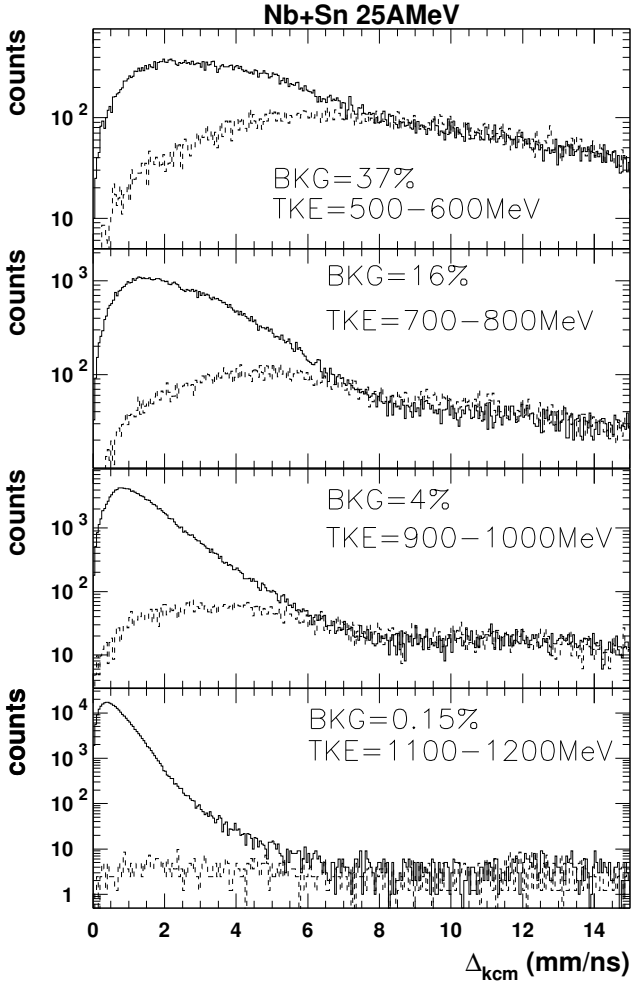


Fig. 3. Spectra of the Δ_{kcm} for the quoted bins of TKE for the reaction $^{93}\text{Nb}+^{116}\text{Sn}$ at 25 AMeV; the full curve refers to the measured 2-body events while the dashed one represents the estimated background due to incompletely detected 3-body events. The quoted percentage of the background contribution refers to the region below $\Delta_{kcm} \approx 8$ mm/ns.

been normalized (by a single normalization factor for all TKEL bins) to the experimental distributions in the tail region. As can be seen, the shape of the long tails at high Δ_{kcm} values is well reproduced, thus lending further support to its interpretation in terms of 3- (or more-)body background.

Only events in the window $\Delta_{kcm} \lesssim 8$ mm/ns, corresponding to the peak of the distribution, were considered in the analysis. Moreover, the contribution of the estimated background was subtracted from the final spectra [29]. This contribution grows with increasing dissipation until, at TKEL of 600-700 MeV, it accounts for almost 30% of the measured events. This is the reason why, in the following, we shall limit our analysis at 2-body events with TKEL $\lesssim 700$ MeV.

2.3.8 Correction for intrinsic and geometric efficiency

In order to obtain meaningful results, all experimental distributions need to be corrected for “instrumental” and physical effects, due not only to the finite resolution of the measurement and possible biases of the analysis, but also to the smearing of the particle evaporation process. As an example, the average values deduced from nonuniformly distributed variables may be severely biased, due to finite resolution effects, unless proper corrections are applied (see, *e.g.*, the comment about angular distributions in [29] and the correction of mass distributions in [31]).

Moreover, it is worth noting that the quantities of physical interest (like, *e.g.*, masses, angles or dissipated energy), although derived from truly uncorrelated parameters measured by the detectors (*e.g.*, time-of-flight, x-y position, deposited energy and so on), acquire a certain degree of correlation [31], which must be corrected for.

In general the corrections are rather involved and may be worked out analytically only in very simple cases. Therefore in the present work the experimental results were corrected via extensive Monte Carlo simulations, modeling the dissipative collision followed by an evaporative emission and incorporating as realistically as possible the response of the setup, finite resolution effects and distortions of the analysis method.

The parametrization of the dissipative collision was tuned in such a way that the simulated distributions, after passing the experimental filter, reproduced the experimental ones. For the evaporative step, thermal emission (leading to Maxwellian energy distributions) was assumed, until the excitation energy of the emitter was exhausted. The multiplicity of light particles was tuned on the results of statistical model calculations with the code GEMINI [27], while the multiplicity of intermediate mass fragments (IMF) had to be somewhat enhanced to reproduce the data (see later in sect. 3.1.3). More details about the simulation can be found in the Appendix and in ref. [1].

3 Data analysis and experimental results

An estimate of the sharing of excitation energy between the two reaction products of a binary dissipative collision can be performed by detecting also the emitted light particles. An alternative, and in many respects complementary, method consists in the simultaneous estimate of the primary (or pre-evaporative) mass A and secondary (or post-evaporative) mass A_{sec} of the products of a binary collision, so that the total number of emitted nucleons can be obtained from the difference between these two values, $\Delta A = A - A_{sec}$. At the cost of no information whatsoever on the various particle species, this method yields the global number of nucleons (irrespective of energy, emission angle and species of particle) which were lost by the investigated fragments.

This method was applied in the past to measurement of PLF from rather asymmetric systems studied in direct kinematics only [12, 25, 15] and required a detailed and not trivial comparison between the experimental results and

evaporation calculations. To avoid relying on model calculations (which become increasingly uncertain with increasing excitation energy), we aimed at comparing not the data with a model, but directly two sets of experimental data.

With an asymmetric colliding system, one might compare the two event samples in which reaction products of a given mass A are PLF or TLF, this fact implying different "histories" (gained or lost nucleons). To overcome the severe experimental difficulties (like threshold effects, poor resolution, and critical dead layer corrections) which impede the measurement of the secondary mass of the TLF with sufficient accuracy, we devised the alternative approach of measuring the secondary mass of the PLF only, however studying the same asymmetric collision both in direct and reverse kinematics. This approach gives also the additional bonus that the efficiencies for the detection of the PLF, being quite similar for the two kinematics, practically do not affect the result of the comparison.

3.1 Experimental results on total evaporated mass

3.1.1 General features

The two most abundant event types are those with two or three heavy fragments in the exit channel. Their relative importance is shown in fig. 4, where the two yields are plotted as a function of TKE for the reaction $^{93}\text{Nb}+^{116}\text{Sn}$ at 25 AMeV, after correction for the efficiency of the set-up by means of Monte Carlo (MC) simulations. As can be seen, the binary exit channel accounts for most part of the total reaction cross section, but the ternary channel is dominant at low TKE values.

The gross features of the binary events resemble those of the well known deep-inelastic reactions at lower bombarding energies (fig. 5). The distribution of TKE extends continuously from quasi-elastic energies down to very low

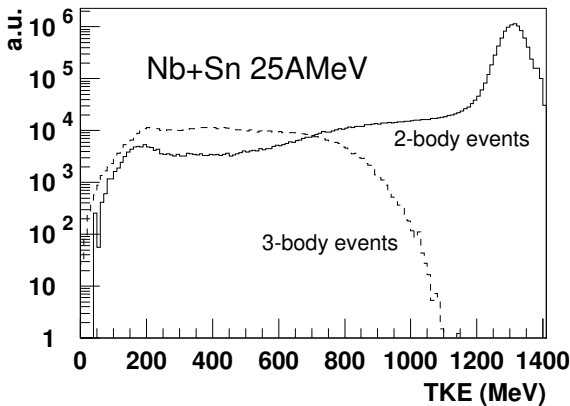


Fig. 4. Distributions of 2- (solid line) and 3-body (dashed line) events as a function of TKE for the reaction $^{93}\text{Nb}+^{116}\text{Sn}$ at 25 AMeV. The data are corrected for the different detection efficiencies of the two exit channels via Monte Carlo simulations.

values, roughly corresponding to the Coulomb repulsion of two nuclei at contact.

The angular distribution of PLF is strongly focused near or below the grazing angle for events in a wide range of TKE values (down to about 500 MeV), corresponding to partly relaxed events. Only fully relaxed events present a broad and nearly flat angular distribution, which is suggestive of a possible orbiting behavior.

Concerning the primary mass distributions, at the end of the interaction the two reaction products maintain, on the average, their original mass value, but the variance of their mass distribution undergoes a rapid growth when passing from peripheral collisions to more central ones. This latter fact can be seen in fig. 6 which shows, as a function of TKEL, the variance σ_A^2 (open symbols) of the primary (MC corrected) mass distribution of PLF from the reaction $^{93}\text{Nb}+^{116}\text{Sn}$ at 25 AMeV, measured in direct and reverse kinematics. The variances are obtained from Gaussian fits to the primary mass distributions obtained with the kinematic coincidence method.

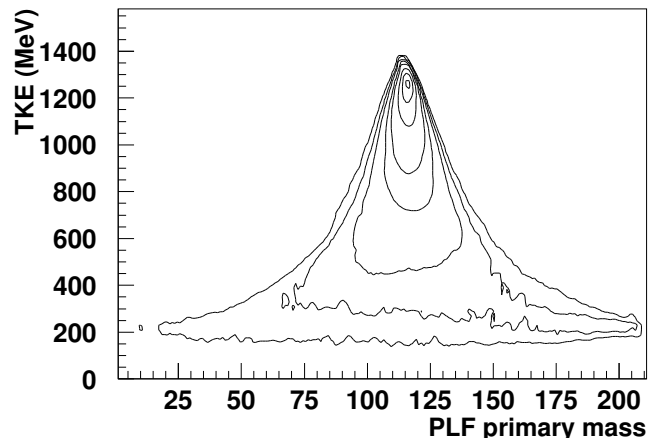
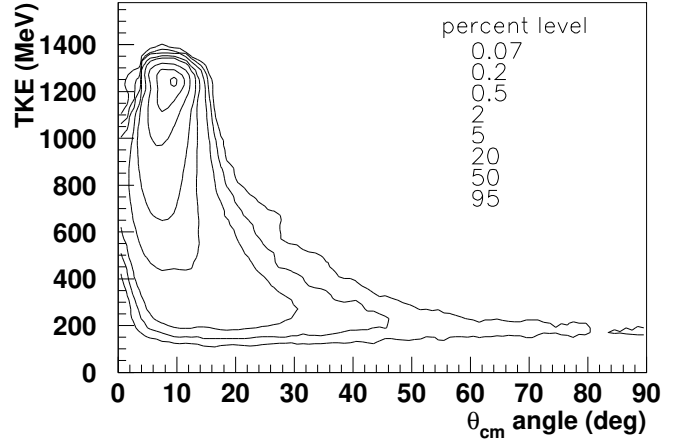


Fig. 5. Experimental correlations $\frac{d^2\sigma}{dTKE d\theta_{\text{PLF}}^{\text{cm}}}$ (Wilczynski-Plot, upper part) and $\frac{d^2\sigma}{dTKE dA_{\text{PLF}}}$ (Diffusion-Plot, lower part) for the system $^{93}\text{Nb} + ^{116}\text{Sn}$ at 25 AMeV, not efficiency corrected.

3.1.2 Mass variances, ΔA , Δ_{kcm}

In particular, as a good estimate of primary masses was of paramount relevance in this work, a great effort was devoted to a better understanding of possible distortions which may affect the measurement of primary masses. Although we correct for these effects with Monte Carlo methods, it can be shown that the distributions of reconstructed primary mass are dominated by the physical width and not by the “instrumental” resolution, so that the corrections are small. For comparison, fig 6 shows the contribution to the variances due only to the evaporation, detection and reconstruction effects (stars in the figure). It was estimated by assuming, in the Monte Carlo simulation, that the primary masses in the exit channel were those of projectile and target. As can be seen, this contribution to the observed mass variance is always of the order of 25% or smaller. Thus, from the simple formula proposed in [31], one can get a quick idea about the errors affecting the uncorrected primary-mass values. Assuming $A=93$ for the most probable exit mass of the PLF, an uncorrected value of $A=103$ would be overestimated by 2 amu, at most.

In fig. 6 we also show (full line) the mass variances obtained from Monte Carlo simulations, when using the parameterization proposed by Gralla et al. [32] for similar mass systems at lower bombarding energies, with the values of the parameters tuned to better reproduce the experimental widths at 25 AMeV (for the exponential slope parameter in eq. 1 of [32], a value of $-4.3 \hbar/\text{MeV}$ was used instead of -5.27).

In dissipative collisions, large amounts of excitation energy are deposited in the outgoing primary fragments,

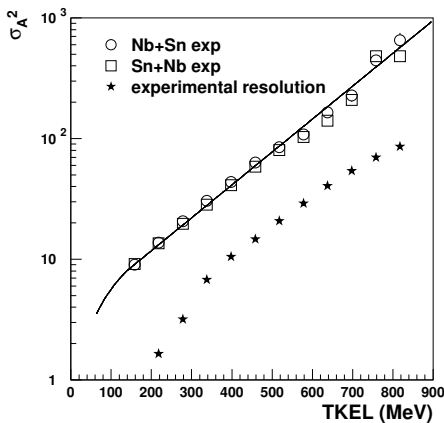


Fig. 6. Experimental variances σ_A^2 of the primary mass distributions of PLF, as a function of TKEL, for the collision $^{93}\text{Nb}+^{116}\text{Sn}$ at 25 AMeV, both in direct and reverse kinematics. PLF masses and TKEL were estimated with the kinematic coincidence method and the variances were obtained with Gaussian fits after efficiency correction. The full line shows the parametrization of the variances used in the Monte Carlo simulations for the efficiency corrections. The stars represent the contribution to the variances due to evaporation, detection and reconstruction, as deduced from Monte Carlo simulations.

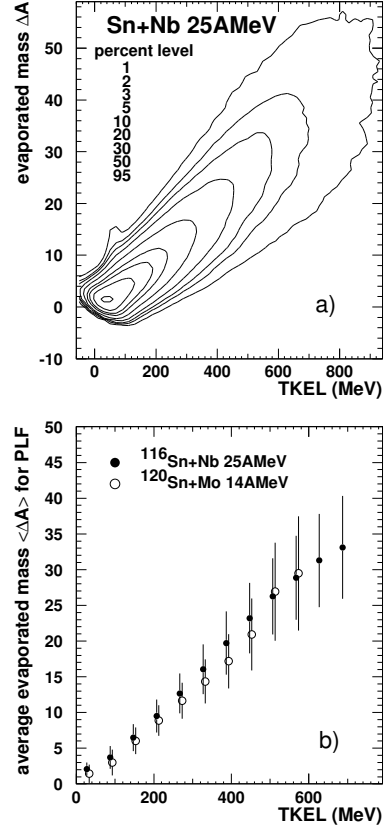


Fig. 7. a): Distribution of the difference $\Delta A = A - A_{\text{sec}}$ between primary and secondary mass of the PLF as a function of TKEL for the reaction $^{116}\text{Sn} + ^{93}\text{Nb}$ at 25 AMeV. The data are not efficiency corrected. The shape of the distribution in the (quasi-)elastic region is due to the finite resolution and to the correlations arising from the use of the measured time-of-flight for the estimation of masses and TKEL. b): Average value of ΔA for different windows of TKEL in the collisions $^{116}\text{Sn}+^{93}\text{Nb}$ at 25 AMeV (full circles) and $^{120}\text{Sn}+^{100}\text{Mo}$ at 14 AMeV (open circles). The vertical bars represent the second moments of the distributions.

which de-excite mainly by evaporation of light particles. This feature is clearly apparent in fig. 7a which shows, for the reaction $^{116}\text{Sn}+^{93}\text{Nb}$ at 25 AMeV, the measured correlation (not Monte Carlo corrected) between the total number of nucleons emitted by the PLF, $\Delta A = A - A_{\text{sec}}$, and TKEL. These results are integrated over all PLF masses. The weak tail extending towards large values of ΔA at small TKEL, is what remains of the elastic projectiles punching through the wires of the gas counters (see sect. 2.3.5) after the subtraction of this background. This plot looks quite similar to that reported in fig. 1 of the paper by Kwiatkowski et al. [25]. In the present case, however, the de-excitation of nuclei with much larger excitation energies can be studied, at TKEL values as large as ≈ 700 MeV, where up to about 50 nucleons are lost by the PLF. By cutting the bidimensional distribution of fig. 7a into vertical slices, one obtains the average values of ΔA as a function of TKEL presented by the full circles in part b) of the same figure, with the vertical bars representing the

second moments. For comparison, the same figure shows as open circles also the ΔA of PLF produced in the reaction $^{120}\text{Sn}+^{100}\text{Mo}$ at 14 AMeV [9]. The data at the two bombarding energies practically coincide, as it has to be for an evaporative process if TKEL is a good estimate of the total excitation energy of the system and ΔA a good estimate of the excitation energy of the PLF. This fact can be taken as an indirect evidence that, at 25 AMeV and for relatively large impact parameters, pre-equilibrium effects still do not play a major role. In fact, in nearly symmetric collisions of heavy nuclei, on average, the center-of-mass of the interacting system after pre-equilibrium emission is not expected to be appreciably different from the center-of-mass of the entrance channel. The main effect of pre-equilibrium on the kinematic reconstruction should then be an overestimation, by a common scaling factor, of the true values of E_{cm} , TKE and A . As a consequence the difference $\Delta A = A - A_{\text{sec}}$ should be much more strongly affected than $\text{TKEL} = E_{\text{cm}} - \text{TKE}$ and this seems not to be the case in fig. 7b.

3.1.3 Intermediate mass fragments

Figure 8 shows the shape of the experimental distributions of ΔA (full histograms) for several TKEL windows. The spectra were obtained by projecting TKEL-slices of fig. 7a onto the vertical axis, but with the additional condition that the primary mass A be in a narrow window around the mass of the projectile, namely at 116 ± 2 . With increasing TKEL, the maximum of the distributions moves to larger values and the width increases, while an evident tail towards large values of ΔA is present at all TKEL. This can be considered as an indirect evidence for the emission of Intermediate Mass Fragments (IMF) which may be important especially in the tail of the distributions towards large ΔA values. With respect to light particles, IMF have a larger binding energy per nucleon and in a thermal process they are emitted with lower kinetic energy per nucleon. Therefore, for a given total emitted mass, they should be less effective in removing excitation energy. Thus, a nucleus of a given mass and excitation energy which evaporates one or more IMF is likely to end up with a smaller secondary mass (and hence a larger ΔA).

Indeed, a good reproduction of the experimental distributions was obtained when including in the evaporation step of the Monte Carlo simulation not only the emission of light particles, but also of IMF (actually we took just Li and C nuclei as representative of all IMF). Their multiplicity, linearly rising with excitation energy, was tuned to reproduce the data and the final results are shown by the dashed histograms in fig. 8. The adopted values correspond to total multiplicities of IMF about 3 times larger than predicted by the statistical code GEMINI. In order to put into evidence the importance of IMF for reproducing the tail on the right side of the distributions, we run also a simulation featuring the statistical emission of light particles only (dotted histograms). While the position of the most probable value and the shape of the left side of the experimental distributions are rather well reproduced,

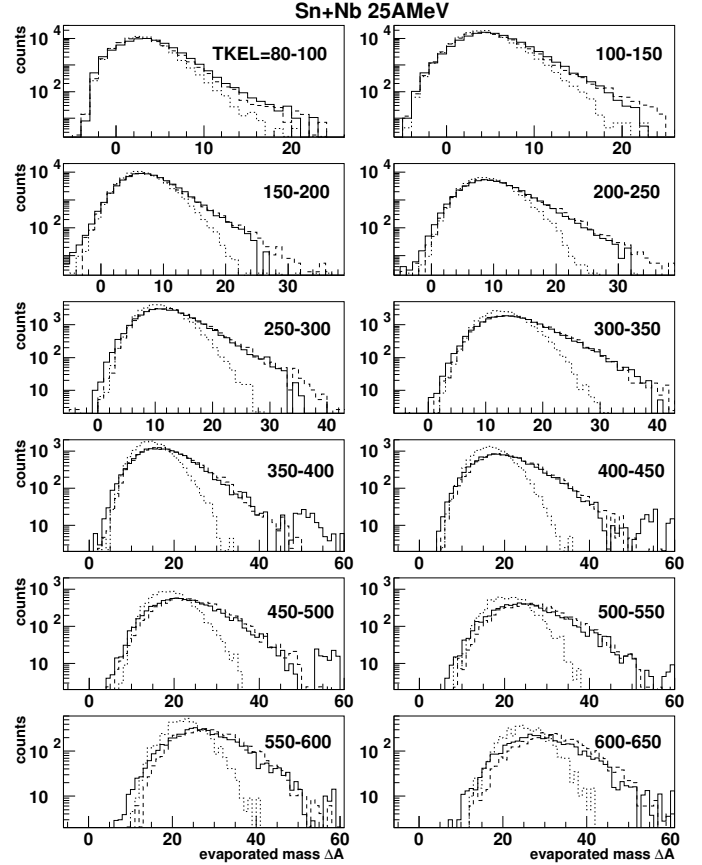


Fig. 8. Shape of the distributions of ΔA for different bins of TKEL from the reaction $^{116}\text{Sn} + ^{93}\text{Nb}$ at 25 AMeV. Shown are the spectra for the experimental data (full histograms), the results of a Monte Carlo simulation featuring only evaporation of light particles (dotted histograms) and the results of a Monte Carlo simulation including also the emission of IMF, tuned to reproduce the experimental data (dashed histograms). Note the changes of abscissa.

the tail on the right side is not reproduced at all. At low TKEL it underestimates the experimental data and with increasing TKEL the obtained distributions tend to become even more symmetric.

Of course mechanisms other than statistical emission may contribute and indeed, at somewhat larger bombarding energies, IMF emission from the “neck” region has been observed (see, *e.g.*, refs. [33,34]). However, the effect of IMF emission on the shape of the ΔA distribution is indirect and not very sensitive to the assumed mechanism, so no attempt to refine the simulations was done.

Indirect evidence for an increased emission of IMF can be obtained not only from the shape of the total emitted mass ΔA , but also from the perturbation of the 2-body kinematics. In fact, the recoil effects due to the IMF emission represent a sizeable perturbation and are visible also in the increased width of the distribution of Δ_{kcm} (see sect. 2.3.1). Figure 9 shows the shape of the experimental distribution of Δ_{kcm} (full histogram) in one bin of TKEL, compared with the result of the Monte Carlo simulation

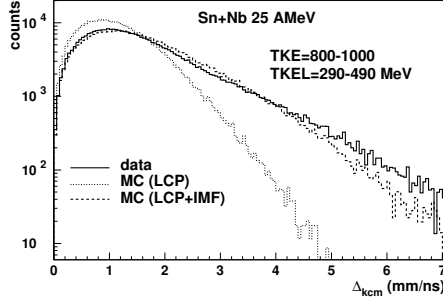


Fig. 9. Shape of the distribution of Δ_{kcm} in one bin of TKEL from the reaction $^{116}\text{Sn} + ^{93}\text{Nb}$ at 25 AMeV. As in the previous figure, full, dotted and dashed histograms represent experimental data, MC simulation with evaporation of light particles only and MC simulation including also the emission of IMF, respectively.

(dashed histogram) which well reproduces the data of fig. 8 and is characterized by an increased evaporation of IMF with respect to GEMINI. Again, to stress the importance of IMF emission, the dotted histogram shows the result of the simulation featuring the emission of light particles only. The reproduction of the experimental shape is still not perfect, but nevertheless the comparison shows the need for large perturbations of the kinematics, which in the present case have been obtained through the simulation of statistical emission of IMF.

3.1.4 Correlation between ΔA and A

In order to study the partition of the excitation energy between the two outgoing heavy fragments of the reaction, the experimental data were sampled in bins of reconstructed primary mass A of the PLF, for various windows of TKEL (corrected for Q_{gg} , the Q -value between ground-states in the entrance and exit channels [10]). The centroids of the corresponding distributions of evaporated mass $\Delta A = A - A_{\text{sec}}$ were then determined. The open squares and open circles in fig. 10 present ΔA (without corrections) as a function of the primary mass of the PLF in the direct and reverse reaction, respectively. The data are shown for three bins of TKEL corresponding to partly damped events, where PLF can be safely distinguished from TLF due to the strongly anisotropic angular distributions [1]. The full symbols in fig. 10 show the same experimental data after correction via Monte Carlo simulation.

It has to be noted at this point that the applied corrections are indeed small (in most cases less than 1–2 amu). Moreover they are largely independent (within errors) of physical hypothesis (*e.g.* on energy partition), as it was checked by repeating the Monte Carlo simulations with different physical models. The corrections are largest (up to 4–5 amu) for the lightest masses at small TKEL, where the uncorrected data display, for the lowest masses, a kind of upward turn. This shape is the result of finite-resolution effects, mainly in the time-of-flight observable. It was already pointed out by the authors of ref. [31] that their

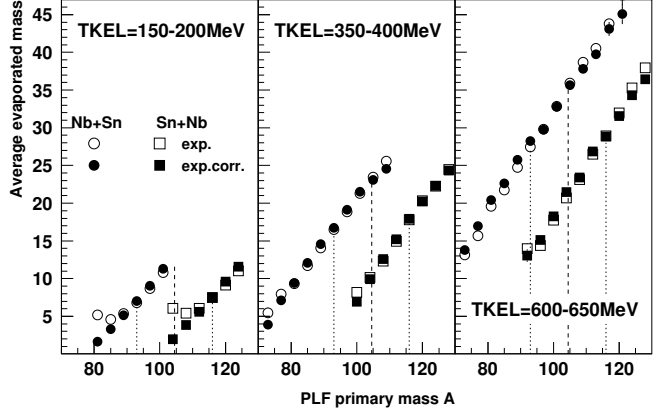


Fig. 10. Experimental average number of evaporated nucleons ΔA as a function of the primary mass A of the PLF in the direct (open circles) and reverse reaction (open squares) at 25 AMeV, for three windows of TKEL. The full symbols show the experimental data after correction for the response of the setup, finite resolution effects and distortions of the analysis.

eq. (8), which had been worked out for the analysis of the reconstructed primary mass distributions in the collision $^{56}\text{Fe} + ^{165}\text{Ho}$ at 9 AMeV, just corrects each bin of a non-uniform distribution for the unequal contributions coming from the neighboring bins located to its right and to its left. Such a simple correction is justified only when the correlations among variables are negligible. In more complex cases, proper corrections can be performed only with the help of realistic Monte Carlo simulations, and this is the method applied in our analysis.

Monte Carlo simulations showed that in our experiment, where the nuclei collide with large relative velocities, at low values of TKEL the time-of-flight resolution of the PLF is the most critical parameter. Not only it mainly determined the resolution of the three variables used in fig. 10 — namely A , A_{sec} (used to build $\Delta A = A - A_{\text{sec}}$) and TKEL — but, being a common ingredient of them all, it also introduced correlations among them. For example, A was positively correlated with A_{sec} (leading to a partial compensation in ΔA) and with TKEL, however the details of these effects could be investigated only with Monte Carlo methods.

The data of fig. 10 present two distinct correlations between the average number of emitted nucleons ΔA and the primary mass A for the two kinematic cases. When properly corrected, these correlations appear to be approximately linear and almost parallel. This finding is similar to the one already observed in the system $^{100}\text{Mo} + ^{120}\text{Sn}$ at 14 AMeV [9]. Also in the present case, the most striking feature resides in the different observed values of ΔA , depending whether they refer to PLF produced in the direct Nb+Sn or in the reverse Sn+Nb reaction. This is a direct evidence for a dependence of the average number of emitted nucleons on the net mass transfer.

3.2 Experimental results on light charged particles

The purpose of the scintillator array “Le Mur” was to determine the average multiplicity of light charged particles (LCP) to be attributed to the PLF. As already stated, a first selection removed all particles stopped in the scintillator material. The remaining particles were then cleanly identified by charge Z , so that in the following we will refer just to hydrogen and helium ions, as their isotopic composition could not be determined with the employed experimental set-up. Due to the limited range of laboratory angles ($\theta_{\text{lab}} \leq 18.5^\circ$) covered with “Le Mur” in the present configuration, only a part of the angular distribution of the light particles in the frame of the emitter could be measured.

A first general selection of the data was performed by requiring that the light particles be emitted on the other side of the beam with respect to the PLF Silicon detectors, to avoid the complicated corrections due to their shadows. Further, in order to study the shape of the LCP velocity spectra, a forward angular range in the PLF frame was selected, such that the geometric acceptance of the scintillators did not appreciably bias the experimental data. This range was determined with the help of Monte Carlo calculations employing realistic velocity distributions, by requiring that the velocity distributions of the LCP before and after the experimental filter had the same shape, within errors. It was found that the best angular range was $\theta=18^\circ\text{--}34^\circ$ and $42^\circ\text{--}54^\circ$ for hydrogen and helium particles, respectively.

In fig. 11 some experimental velocity spectra of LCP in the so determined angular range in the PLF frame (circles) are compared with the unfiltered results of evaporation calculations, obtained from the statistical code GEMINI (histograms) with appropriate excitation energies. The left and right columns of the figure are for hydrogen and helium ions, respectively. The first and second row refer to two windows of TKEL for the exit channel without net mass transfer in the collision $^{116}\text{Sn} + ^{93}\text{Nb}$. The third row is for the exit channel leading to symmetry, either by a net loss of nucleons (left panel, mass $A=104$ in the collision $^{116}\text{Sn} + ^{93}\text{Nb}$) or by a net gain of nucleons (right panel, mass $A=104$ in the collision $^{93}\text{Nb} + ^{116}\text{Sn}$). It can be seen that the agreement between experimental data and calculations is rather good thus showing that the estimated excitation energies are correct and that, in the chosen angular range, the data are indeed rather unbiased and compatible with a thermal emission.

Some trends, which will be explained in more detail in the following, are visible already in fig. 11. The comparison of left and right columns shows that the velocity distributions for hydrogen are generally broader than those for helium, having larger mean value, variance and skewness. The widths slightly increase with increasing TKEL (compare the first and the second row), whereas for a given TKEL they tend to increase or decrease for a net gain or loss of nucleons (compare the second and third row). Unfortunately the extraction of an (apparent) temperature of the emitting source would be ambiguous. In fact, the ΔE vs. ToF identification technique does not give any in-

formation about the mass of the detected particles. This fact prevents a reliable transformation of the velocity distributions into energy distributions, especially for $Z=1$ particles, where comparable contributions from protons, deuterons and tritons are expected.

Now an analysis similar to that of sect. 3.1.4 can be performed also with the data of the light charged particles [35]. To do this, the average multiplicity $\langle M_{\text{LCP}} \rangle$ of hydrogen and helium ions was determined as a function of the primary mass A of the detected PLF, for different windows on TKEL. In order to improve the statistics, a wider range from about $\theta=14^\circ$ to 70° in the emitter frame was used. Monte Carlo simulations showed that set-up was still reasonably efficient in this range. In this way, the relative multiplicity of light charged particles emitted by PLF of different primary masses A is relatively free

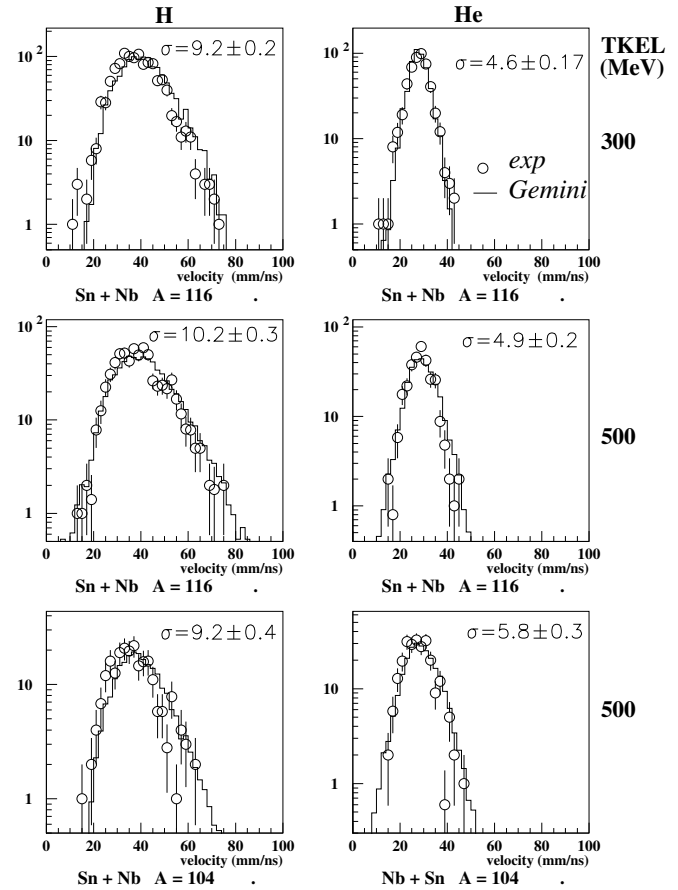


Fig. 11. Selected experimental spectra of the velocity of light charged particles in the PLF frame (circles) and results of evaporation calculations with the statistical code GEMINI (histograms). The left and right columns show results for hydrogen and helium ions, respectively. The first and second row are for two windows of TKEL for the exit channel without net mass transfer in the collision $^{116}\text{Sn} + ^{93}\text{Nb}$, while the third row refers to the exit channel leading to symmetry, either by a net loss of nucleons (left panel, mass $A=104$ in the collision $^{116}\text{Sn} + ^{93}\text{Nb}$) or by a net gain of nucleons (right panel, mass $A=104$ in the collision $^{93}\text{Nb} + ^{116}\text{Sn}$). The widths σ of the distributions were deduced from their second moments.

of bias, whereas the absolute values are somewhat more uncertain, because the extrapolation to the whole solid angle relies on assumptions about their in-plane and out-of-plane distributions.

The left and right columns of fig. 12 present the obtained results (efficiency corrected with Monte Carlo simulations) for hydrogen and helium ions, respectively, in three windows of TKEL. The circles and squares refer to the multiplicities of light charged particles emitted from the PLF in the $^{93}\text{Nb} + ^{116}\text{Sn}$ and $^{116}\text{Sn} + ^{93}\text{Nb}$ reaction, respectively. The full symbols show the experimental data corrected under the assumption of a non-equilibrium excitation energy sharing (dependent on the net mass transfer), as deduced from the analysis of fig. 10 (see sect. 4.2 for details). The open symbols show the same experimental data after correction with an energy sharing mechanism independent of the net mass transfer. It is apparent that the results are very insensitive to the particular physical hypothesis on energy sharing used for the correction.

The light charged particle multiplicity $\langle M_{\text{lcp}} \rangle$ presents a general tendency to increase with increasing primary mass A of the emitting PLF. We want to focus attention on the fact that, in a given TKEL window, the multiplicities for the symmetric exit channel are quite different in

the two kinematic cases, although the mass of the emitting PLF is the same ($A \approx 104$). They are larger in the direct reaction, where the PLF has gained mass, with respect to the reverse reaction, where it has lost an equal amount of nucleons. This finding is qualitatively in good agreement with the results already presented in fig. 10 for the total number of evaporated nucleons, ΔA , deduced on the base of a kinematic reconstruction. Thus also the emission of light charged particles shows a clear evidence for a correlation with the number of net transferred nucleons. This behavior is evident (beyond errors and uncertainties) at all TKEL values in case of helium ions, whereas for hydrogens it becomes weaker with increasing TKEL. An interpretation of this fact will be given later in the paper (see sect.4.3).

It is finally worth noting that the measurements of light charged particles in the scintillator array “Le Mur” and of heavy reaction products in the gas detectors are completely independent. Therefore $\langle M_{\text{lcp}} \rangle$ and A in fig. 12 are free from the “instrumental” correlations affecting ΔA and A , as discussed in sect.3.1.4.

4 Discussion

4.1 Energy sharing without net mass transfer

A first information on the average partition of excitation energy between the two reaction partners can be deduced — in a substantially model-independent way — from the number of nucleons emitted in case of no net mass transfer, *i. e.* in the present work for $A=93$ (116) in the direct (reverse) kinematics, respectively. The comparison between the two kinematic cases can be performed [9] on the basis of a dimensionless parameter, C_F , representing the asymmetry in their global evaporation of nucleons¹:

$$C_F = (\Delta A_{116}^h - \Delta A_{93}^l) / (\Delta A_{116}^h + \Delta A_{93}^l) \quad (1)$$

where ΔA_{93}^l (ΔA_{116}^h) is the total number of nucleons evaporated from nuclei of primary mass $A=93$ (116) originating from the entrance channel light (heavy) nucleus. Assuming a common value ϵ for the average energy necessary to evaporate a single nucleon from the two reaction partners, C_F is also an estimate of the asymmetry in excitation energy partition $(E_{116}^{*h} - E_{93}^{*l}) / (E_{116}^{*h} + E_{93}^{*l})$. The open circles in fig. 13 show, as a function of TKEL, the value of C_F obtained from the present experimental data. In the same figure, the dashed line at $C_F=0$ and the dotted one at $C_F \approx 0.11$ indicate the values expected for equal energy and equal temperature sharing, respectively.

One can see that the so estimated average energy partition is fairly constant up to the highest accessible degree of inelasticity (TKEL ≈ 700 MeV). If taken at its face value, the displacement of C_F from zero (with the Sn fragments taking more than half of the total available excitation energy) would point to a situation intermediate between equal energy and equal temperature sharing,

¹ The subscript F indicates a slightly different definition with respect to the parameter C of ref. [15]

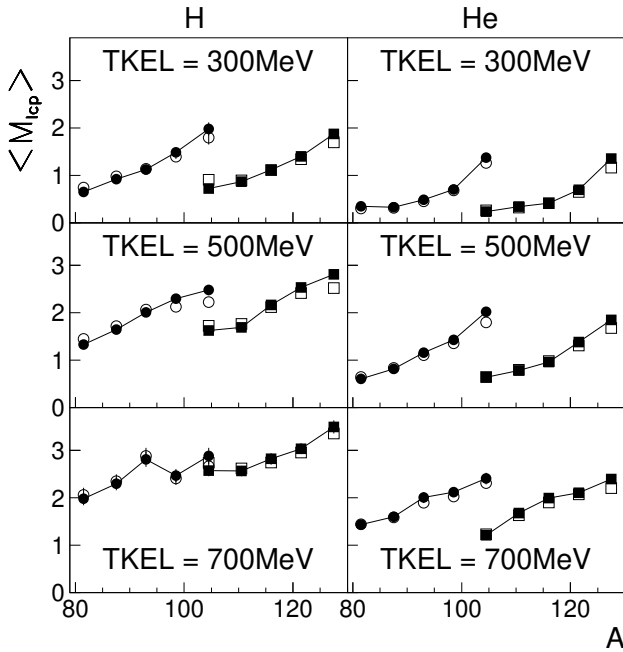


Fig. 12. Efficiency corrected experimental multiplicities for hydrogen (left column) and helium particles (right column) emitted by the PLF, plotted as a function of the primary mass of the PLF and for three windows of TKEL. The circles and squares refer to the multiplicities of light charged particles emitted from the PLF in the $^{93}\text{Nb} + ^{116}\text{Sn}$ and $^{116}\text{Sn} + ^{93}\text{Nb}$ reaction, respectively. The full and open symbols show the experimental data corrected assuming a non-equilibrium excitation energy sharing as deduced from the analysis of the data, and an energy sharing mechanism independent of the net mass transfer, respectively. The lines are drawn just to guide the eye.

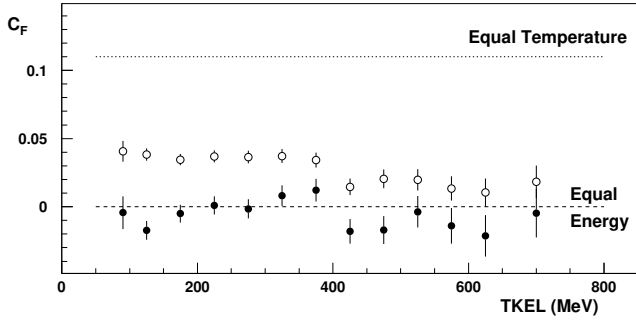


Fig. 13. Experimental asymmetry C_F of the total mass evaporated by the two reaction partners in case of no net mass transfer, as a function of TKEL (see text). The data refer to the asymmetric collision $^{93}\text{Nb} + ^{116}\text{Sn}$ at 25 AMeV. The open points show the data corrected with Monte Carlo calculations taking into account the effects of the analysis method. The full points represent the same data further corrected with the results obtained from an analysis of the symmetric systems. The dashed line at $C_F = 0$ corresponds to the equipartition of excitation (equal energy sharing), while the dotted line shows the value expected for thermal equilibrium (equal temperature sharing).

even at low TKEL values. However, before drawing any conclusion, one should investigate the effects of a possible small dependence of ϵ on the mass (and charge) of the decaying nucleus. To do this, we took advantage of the data obtained, during the same experiment, for the two mass-symmetric systems $^{93}\text{Nb} + ^{93}\text{Nb}$ and $^{116}\text{Sn} + ^{116}\text{Sn}$ at the same bombarding energy of 25 AMeV. In fact, in the symmetric exit channel of symmetric colliding systems, the PLF must take on average just half of the total excitation energy. Then one can readily estimate the average energy ϵ_{93} spent by the ^{93}Nb nuclei to evaporate one single nucleon, $\epsilon_{93} = \frac{1}{2} \text{TKEL} / \Delta A_{93}^{\text{sym}}$ (and in a similar way ϵ_{116} for the ^{116}Sn nuclei). The superscript "sym" stresses that we refer here to symmetric colliding systems. The average cost to evaporate nucleons from Nb nuclei was $\epsilon_{93} \approx 11\text{--}12$ MeV depending on excitation energy, while the value for Sn nuclei was found to be systematically lower by about 0.7 MeV. All these values are compatible with statistical model calculations.

It is perhaps worth noting that pre-equilibrium emission, if present, might somewhat alter the absolute values of the so obtained ϵ_{93} and ϵ_{116} , but to a much lesser extent their difference. Moreover, the effects of pre-equilibrium emission in the symmetric and asymmetric systems tend to cancel when applying such a correction to C_F . The so deduced small differences of ϵ between Nb and Sn nuclei were used to correct the estimate of C_F in the asymmetric systems, by multiplying each term ΔA in eq. 1 with the appropriate ϵ value. The full circles in fig. 13 show C_F vs. TKEL after correction. Within errors, the excitation energy is now shared equally between the reaction products.

In previous works in the literature [24,17], referring to more asymmetric systems at lower bombarding energies, the excitation energy was found to be almost equally shared between the colliding nuclei for small TKEL (cor-

responding to a wide range of peripheral impact parameters), while the thermal limit was slowly approached – but never reached – with increasing TKEL. Such a behavior has been qualitatively well understood in the framework of nuclear exchange models. Due to their randomness, the first exchanges of nucleons are predicted to produce about the same amount of excitation energy in the two cold nuclei: the larger the mass asymmetry of the colliding nuclei, the stronger the thermal non-equilibrium developing in this first phase of the interaction. However, this thermal disparity leads to a change of the fluxes of nucleons between the partners of the reaction and drives the dinuclear system towards thermal equilibrium. Therefore, allowing a long enough duration of the contact phase (as it may happen at small impact parameters and at low bombarding energies), the statistical decay of the two outgoing fragments should be consistent with thermal equilibrium (equal temperature condition).

The data in this paper are the first on this subject at these higher bombarding energies. The striking feature is that C_F presents no evidence of an (even slow) trend towards the equal temperature limit (dotted line in fig. 13) with increasing TKEL. As such, the present data also differ from the results we obtained in a similar experiment at the lower bombarding energy of 14 AMeV (see fig.2b of ref. [9]), where a trend towards the equal temperature partition was indeed found.

An explanation can be sought in the strongly different interaction times τ_{int} at these two bombarding energies. As suggested by different model calculations at 25 AMeV the values of τ_{int} are shorter for a given TKEL and their increase with increasing TKEL is slower. Just as an example, the reaction times calculated in the frame of the Nucleon Exchange Model (lines) [20] and in a Landau-Vlasov approach (symbols) [36] for the two bombarding energies are presented in fig. 14. Referring, for example, to the NEM calculations, one sees that in the collision $^{100}\text{Mo} + ^{120}\text{Sn}$ at 14 AMeV $\tau_{\text{int}} \approx 200$ fm/c is obtained already at TKEL $\approx 300\text{--}400$ MeV, but similar interaction times are reached only at TKEL $\approx 800\text{--}900$ MeV in the collision $^{93}\text{Nb} + ^{116}\text{Sn}$ at 25 AMeV. The present indica-

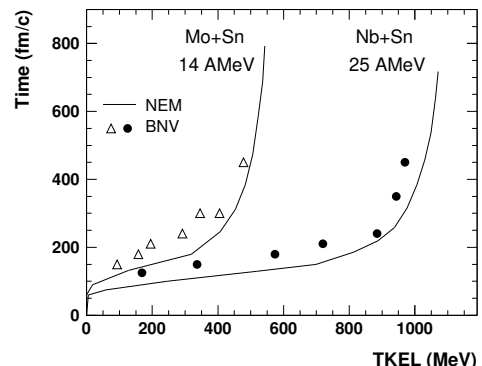


Fig. 14. Reaction times calculated in the frame of the Nucleon Exchange Model (lines) and in a Landau-Vlasov approach (symbols) for the systems $^{100}\text{Mo} + ^{120}\text{Sn}$ at 14.1 AMeV and $^{93}\text{Nb} + ^{116}\text{Sn}$ at 25 AMeV.

tion is in agreement with the result of ref. [4] which claims that in the asymmetric system $^{40}\text{Ar} + ^{\text{nat}}\text{Ag}$ at 27 AMeV energy equilibration is not obtained for interaction times shorter than 180 fm/c.

An experimental, although qualitative, observation in favor of a difference in time scales can be obtained also from the correlations $d^2\sigma/dTKEd\theta_{\text{PLF}}^{\text{cm}}$ (Wilczynski-Plot) measured at the two energies. At 14 AMeV, the highest TKEL at which the parameter C_F could be analyzed corresponds to the attainment of an orbiting condition (implying long interaction times). In the experiments at 25 AMeV, on the contrary, at the highest TKEL values used for determining C_F the PLF deflection angles are still peaked close to the grazing angle, indicating short interaction times even at TKEL as large as 800 MeV.

Additional support to the hypothesis of a lack of statistical equilibrium even at high TKEL can be obtained from the comparison of the data of the collisions $^{116}\text{Sn} + ^{58}\text{Ni}$, $^{116}\text{Sn} + ^{197}\text{Au}$ and $^{116}\text{Sn} + ^{116}\text{Sn}$, all measured at 25 AMeV. The strong mass asymmetry of the first two systems increases the sensitivity of the measurement of ΔA_{116} on the possible evolution of the excitation energy sharing towards equilibrium. Let us consider, for all reactions, the exit channel with $A_{\text{PLF}}=116$ (no net mass transfer). Of course, in case of “equal energy” sharing and for a given TKEL, one expects the same excitation energy of the PLF in the three systems. On the contrary, in case of an evolution towards statistical equilibrium (“equal temperature” sharing), the excitation energy of the PLF is expected to depend on the system, as the mass ratios $A_{\text{proj}}/A_{\text{tot}}$ are very different (116/174 \approx 0.67 for Sn+Ni, 116/313 \approx 0.37 for Sn+Au and 0.5 for Sn+Sn). Therefore, if ΔA_{116} depends just on the excitation energy of the PLF, it should increase differently as a function of TKEL.

Figure 15 shows the experimental ΔA_{116} (uncorrected) for the two strongly asymmetric systems (squares and tri-

angles) together with the results for the symmetric system $^{116}\text{Sn} + ^{116}\text{Sn}$ (circles). The behavior expected for the asymmetric systems in case of “equal temperature” sharing (full and dashed lines for Sn+Ni and Sn+Au, respectively) can be obtained from the data points of the symmetric Sn+Sn system by rescaling their abscissas with the ratios of total masses (116+197)/(116+116) and (116+58)/(116+116), respectively. One sees that, up to the highest explored TKEL, the values of ΔA_{116} for the asymmetric system Sn+Au closely follow the points for the Sn+Sn system, thus suggesting an “equal energy” sharing behavior. Indeed, in the considered TKEL range, NEM calculations give interaction times which are rather short (\lesssim 150 fm/c) and very similar for the two systems. The behavior of the Sn+Ni system, on the contrary, is somewhat different and not fully understood, with data points in between the “equal energy” and the “equal temperature” expectations.

4.2 Energy sharing with net mass transfer

Information on the dependence of the excitation energy sharing on the net mass transfer is carried by the slope of – and by the separation between – the two experimental correlations of fig. 10.

One easily sees that at 25 AMeV the difference of ΔA for a given A in the two kinematic cases amounts to about 11–14 amu, almost independently of TKEL. If there are no violent dynamical effects at work, the emission of particles is essentially of statistical nature and this difference can be ascribed mainly to a different excitation energy of the emitting PLF. This value of ΔA can be converted into an excitation energy using the previously found value of 11–12 MeV for the average energy needed to remove one nucleon. Thus, for $\text{TKEL} \geq 200$ MeV (where the mass distributions of PLF in direct and reverse kinematics have some overlap), the observed difference suggests that a PLF of a given mass A produced in the direct Nb+Sn reaction has about 125–160 MeV of excitation energy more than a PLF of the same mass produced in the reverse Sn+Nb collision. In other words, there is an excitation-energy excess of about 6 MeV per net gained nucleon, averaged over the whole sequence of exchanges leading to the observed final TKEL. We recall that none of the usual ways of modeling the excitation energy sharing – neither the equal-energy, nor the equal-temperature scenarios, nor any combination of the two – foresees the observed existence in the correlation ΔA vs. A of two well-separated lines.

For a given window of TKEL, the experimental correlations of fig. 10 can be treated, to a good approximation, as straight and parallel lines. This implies that the total number of nucleons emitted altogether, $\Delta A_{\text{tot}} = \Delta A_{\text{PLF}} + \Delta A_{\text{TLF}}$, by any pair of reaction partners, $A_{\text{PLF}} + A_{\text{TLF}} = A_{\text{beam}} + A_{\text{target}} = A_{\text{tot}}$, does not substantially depend on the particular exit channel. As in a previous work [9], the dependence of ΔA on the net mass transfer can be described by means of a dimensionless parameter, R_F , representing the asymmetry in evaporated mass for the exit

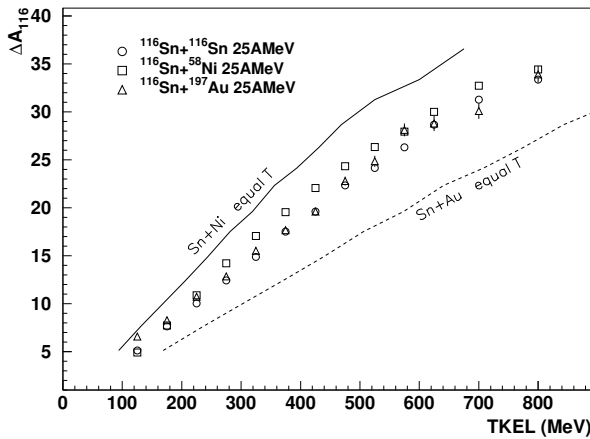


Fig. 15. Experimental evaporated mass ΔA_{116} from excited PLF with $A_{\text{PLF}}=116$ for the three reactions $^{116}\text{Sn} + ^{58}\text{Ni}$, ^{93}Nb and ^{197}Au at 25 AMeV, as a function of TKEL. The full (dashed) line represents an empirical estimate of the ΔA_{116} for an equal temperature sharing in the asymmetric Sn+Ni (Sn+Au) system, based on the data of the symmetric Sn+Sn system.

channel leading to symmetric division of the whole system²:

$$R_F = (\Delta A_{\text{sym}}^l - \Delta A_{\text{sym}}^h) / (\Delta A_{\text{sym}}^l + \Delta A_{\text{sym}}^h) \quad (2)$$

where ΔA_{sym}^l (ΔA_{sym}^h) is the total mass evaporated from nuclei produced in the symmetric exit channel (that with primary masses $A_{\text{sym}} = A_{\text{tot}}/2$), originating from the light (heavy) colliding nucleus – and measured in our experiment as PLF in direct (reverse) kinematics. As already pointed out [9], R_F is also an estimate of the excitation-energy asymmetry $(E_{\text{sym}}^{*l} - E_{\text{sym}}^{*h}) / (E_{\text{sym}}^{*l} + E_{\text{sym}}^{*h})$, in the limit that the small variations of ϵ with excitation energy can be neglected. Since the central mass A_{sym} lies in the wings of the mass distributions where the statistics is lower, R_F was not obtained directly from the data, but deduced from the result of a simultaneous linear fit to the parallel correlations of fig. 10.

Using the expressions eq. 1 and 2 for C_F and R_F , and with a common average value of ϵ , the excitation energy for products of primary mass A^l (A^h) deriving from the original light (heavy) colliding nucleus can be cast in the form [9]:

$$E^*(A^{l,h}) = \left(\frac{1}{2} + \frac{C_F}{A_{\text{dif}}} \left(A^{l,h} - \frac{A_{\text{tot}}}{2} \right) + \frac{R_F}{A_{\text{dif}}} \left(A^{l,h} - A_0^{l,h} \right) \right) TKEL \quad (3)$$

where A_0^l (A_0^h) is the lighter (heavier) mass between A_{beam} and A_{target} in the entrance channel, $A_{\text{tot}} = A_0^l + A_0^h$, $A_{\text{dif}} = A_0^h - A_0^l$ and $TKEL \approx E_{\text{tot}}^*$. Thus, in general, the experimental slope includes a contribution (that with the term C_F) simply describing the dependence of excitation energy on mass, while only the term with R_F truly represents a dependence on net mass transfer and, as such, it is responsible for the existence of two distinct correlations.

The circles in fig. 16a show the obtained values of R_F/A_{dif} as a function of TKEL, together with the results for the systems $^{100}\text{Mo} + ^{120}\text{Sn}$ at 14 AMeV (triangles) and $^{74}\text{Ge} + ^{165}\text{Ho}$ at 8.5 AMeV (crosses). In this latter case, where only the correlation for the direct reaction had been measured, the points were reconstructed on the basis of the measured slopes and of the average partition as estimated in ref. [15]). In all three cases the percentage of excitation energy gained by the net transfer of one nucleon is strongly decreasing with TKEL.

If we consider the product $(R_F/A_{\text{dif}}) \cdot TKEL$, which is the coefficient of the net-mass-transfer dependent term in eq. 3, we obtain the result shown in fig. 16b. At 14 and 25 AMeV this product is roughly constant (or it slightly increases with TKEL), typical values at $TKEL \leq 550$ MeV being 2.5–3 and 5.5–6.5 MeV per net transferred nucleon, respectively. Although only two bombarding energies may be insufficient to draw any stringent conclusion and the observed factor of about 2 between the two experiments might be rather fortuitous, it is worth noting that they

² The subscript F stresses the different definition with respect to the parameter R of ref. [15]

scale like v_{rel}^2 at contact. This observation agrees with the expectations of exchange models where the recoil momentum of the transferred nucleon(s) is the main contribution to the energy dissipated in a single exchange process and the observed correlation with the net mass transfer may arise from an intrinsic asymmetry in the excitation energy generated in the donor and acceptor nucleus at each elementary step. Also BNV calculations [37] at 14 AMeV ascribed such a correlation between total evaporated mass and net mass transfer to an intrinsic asymmetry in the nucleon exchange process.

It has to be noted that in the frame of an exchange picture, one would also expect a flattening [38] of the slope of the correlations ΔA vs A with increasing TKEL (as observed indeed in the collision $^{74}\text{Ge} + ^{165}\text{Ho}$) and hence a decrease of the coefficient $(R_F/A_{\text{dif}}) \cdot TKEL$. In fact, for a given net mass transfer, with increasing TKEL there should be a growing contribution from exchanges taking place at later stages of the reaction, when the relative motion is somewhat slowed down (and hence the dissipated energy per exchanged nucleon is lower). However, rather surprisingly, the experimental data show that $(R_F/A_{\text{dif}}) \cdot TKEL$ does not decrease, on the contrary it is constant or even a weakly increasing function of TKEL.

In the frame of an exchange picture, one would like to have access to the asymmetry in excitation energy at each elementary step:

$$\eta \equiv \frac{e_a - e_d}{e_a + e_d} \quad (4)$$

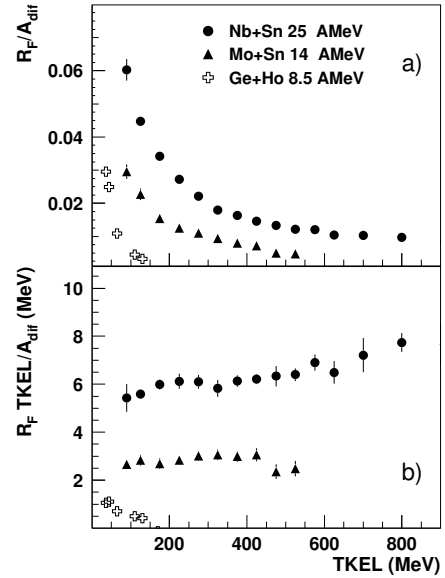


Fig. 16. a): Percentage of excitation energy gained by the net transfer of one nucleon, R_F/A_{dif} , for the systems $^{93}\text{Nb} + ^{116}\text{Sn}$ at 25 AMeV (circles), $^{100}\text{Mo} + ^{120}\text{Sn}$ at 14.1 AMeV (triangles) and $^{74}\text{Ge} + ^{165}\text{Ho}$ at 8.5 AMeV (crosses), as a function of TKEL. b): Coefficient $(R_F/A_{\text{dif}}) \cdot TKEL$ of the net-mass-transfer dependent term in the excitation-energy versus primary-mass parametrization (see text). Same symbols as in part a).

where e_a and e_d are the excitation energy generated in the acceptor and donor nucleus, respectively. Based on some assumptions to be discussed later, Töke et al. [15] proposed an original method to estimate η from the experimental data. Their prescription (see eq. A6 of [15]) can be expressed, employing our parameter notation, in the following way:

$$\eta_{\text{exp}} = \frac{\left(\frac{R_F}{A_{\text{dif}}} \sigma_A^2 \text{TKEL}\right)_{(2)} - \left(\frac{R_F}{A_{\text{dif}}} \sigma_A^2 \text{TKEL}\right)_{(1)}}{C_F(2) - C_F(1)} \quad (5)$$

where σ_A^2 is the variance of the mass distribution and the indices (1) and (2) refer to the experimental data taken from two successive TKEL bins, with $\text{TKEL}(2) > \text{TKEL}(1)$. The quantity η_{exp} is thus, by construction, a differential quantity pertaining to a particular stage of the collision.

In the case of $^{74}\text{Ge} + ^{165}\text{Ho}$ at 8.5 AMeV, Töke *et al.* found that their prescription η_{exp} gave a reasonable value of ≈ 0.3 for the first 100 MeV of TKEL, increasing to about 1 at 130 MeV. This corresponds to an asymmetric sharing of excitation energy in the ratio 1:2 between the donor and the acceptor nucleus. The results of the same prescription applied to the systems $^{93}\text{Nb} + ^{116}\text{Sn}$ at 25 AMeV (circles) and $^{100}\text{Mo} + ^{120}\text{Sn}$ at 14 AMeV (triangles) are displayed in fig. 17 together with the data for the original $^{74}\text{Ge} + ^{165}\text{Ho}$ system at 8.5 AMeV (crosses). In our systems the obtained η_{exp} starts at values around 1 for the lowest TKEL and systematically increases with increasing TKEL, up to values of about 10–20 for the largest TKEL. This fact, of course, prevents the interpretation of η_{exp} as an estimate of the excitation energy asymmetry in a single exchange process. Such a quantity is indeed expected to be bound between +1 and -1, unless one accepts the (unconventional) hypothesis that one of the two nuclei, acceptor or donor, experiences on average a negative variation of excitation energy (*i.e.*, the nucleus becomes systematically colder in an exchange process).

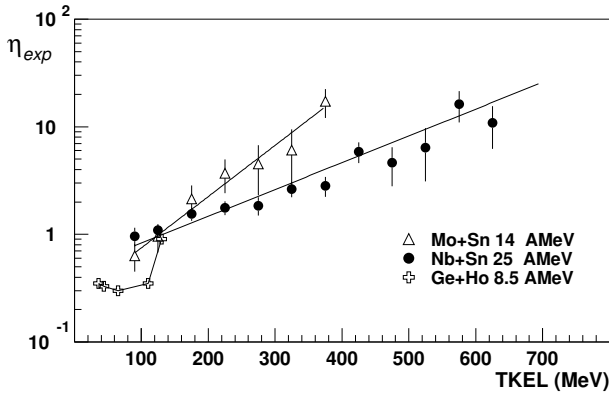


Fig. 17. Value of the experimental quantity η_{exp} , which, in a stochastic nucleon exchange picture, is expected to estimate the excitation energy asymmetry in an elementary exchange process, as a function of TKEL, for the systems $^{93}\text{Nb} + ^{116}\text{Sn}$ at 25 AMeV (circles), $^{100}\text{Mo} + ^{120}\text{Sn}$ at 14.1 AMeV (triangles) and $^{74}\text{Ge} + ^{165}\text{Ho}$ at 8.5 AMeV (crosses).

One is then lead to reexamine critically the assumptions on which the derivation of eq. 5 relies, due to the fact that at high TKEL η appears to be too large by about a factor of 10. Basing on the one-body exchange picture (which portrays the collision as an evolutionary process consisting of a long sequence of elementary steps, each producing a small change of the system) the main assumptions are:

- i) “....collisions leading to different values of E_{loss} evolve along a common path in the space of the relevant collision parameters...” [15];
- ii) in non-central collisions the dissipation mechanism proceeds mainly via the exchange mechanism, with other inelastic or collective excitation modes playing a minor role, if any;
- iii) the dependence of the excitation energy sharing on net mass transfer is quite well approximated by a linear relationship, like for example that of eq. 3;
- iv) the exchange mechanism proceeds through stochastic transfer of single uncorrelated nucleons and the number of exchanges can be deduced from the variances of the mass distribution, $N_{\text{exch}} = \sigma_A^2$.

Point i) implies that the evolution of the relevant quantities (namely, for the present discussion, the number of exchanges, the mass variances and the excitation energy sharing parameters) proceeds along a common path for collisions leading to consecutive bins of TKEL. In other words, the evolution of collisions leading to TKEL and $\text{TKEL} + \Delta\text{TKEL}$ differs only in the final part of the process, the one which is responsible for the additional dissipation ΔTKEL . This is of course an approximation, as “...different values of E_{loss} are expected to involve different partial waves in the entrance channel and, therefore, different system trajectories” [15]. In particular, in the derivation of eq. 5 it is assumed that the number of exchanges in the evolution from TKEL(1) to TKEL(2) is simply given by $\sigma_A^2(2) - \sigma_A^2(1)$.

In order to check how far this approximation is justified, the code for the Nucleon Exchange Model by Randrup [20] was run with the following minor modification. In the original code, the equations of motion of several relevant collective variables are numerically integrated in short time steps along the trajectory of the system and only at the end of the interaction the final values of mass (and charge) variances are estimated. The applied modification performs an estimation of the current mass variance at each integration step, so that it is possible to follow the evolution of σ_A^2 along the (average) trajectory leading to any given final dissipation TKEL. In particular, it is then possible to judge in how far the mass variance $\sigma_A^2(1)$ of a trajectory with final dissipation TKEL(1) is a good estimate of $\sigma_A^2(2 | \text{TKEL}(1))$, that is the mass variance of the trajectory with final dissipation TKEL(2) at the moment when the dissipation had reached the intermediate value of TKEL(1). This is shown in fig. 18, where each curve labeled with the value of the final TKEL in exit channel displays the evolution of σ_A^2 with the dissipated energy along the trajectory. If the hypothesis of i) were rigorously correct, all these curves should fall one on top of the

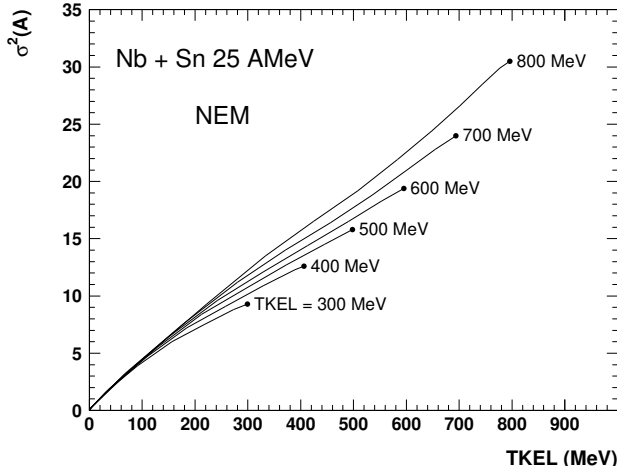


Fig. 18. Evolution of σ_A^2 with the dissipated energy along selected trajectories leading to the indicated final TKEL values, calculated with the Nucleon Exchange Model.

other. One sees that when estimating σ_A^2 in a previous instant on a definite trajectory by means of the final mass variance of a lower curve, one introduces a systematic error of the order of 10% on $\sigma_A^2(1)$. This corresponds to an overestimation of η_{exp} of about 20–30%, at most, and it is therefore insufficient to explain by itself the surprisingly high value of η_{exp} .

The importance of inelastic excitations in the two colliding nuclei (point ii) — either of single particle type or of more collective nature, but not strictly related with a mechanism of nucleon exchanges — has been assessed by some authors in the literature especially for the first phase of the reaction. Assuming that the energy dissipation proceeds partly via such an exchange mechanism and partly via inelastic excitations (not dependent on the net mass transfer), one can still obtain an experimental value of η_{exp} . However in this case only part of the average increase of excitation energy of the nucleus, $\langle E^*(2) \rangle - \langle E^*(1) \rangle \propto C_F(2) - C_F(1)$, is due to the exchange process (this corresponds to adding a term $E_{\text{inelastic}}^*$ to the right hand side of eq. (A5) in ref. [15]). Thus the values of η_{exp} presented in fig. 17, where all dissipation was attributed to an exchange mechanism, would be a lower limit of the excitation energy asymmetry of a single exchange η .

The hypothesis iii) of an approximately linear dependence of the excitation energy sharing on the net-mass-transfer seems quite well supported by the present data (see fig. 10) as well as by the data of the collisions $^{100}\text{Mo} + ^{120}\text{Sn}$ at 14 A MeV [9] and $^{74}\text{Ge} + ^{165}\text{Ho}$ at 8.5 A MeV [15].

It is commonly assumed (hypothesis iv) that the variance σ_A^2 of the experimental mass distributions is a good estimator of the number of elementary exchanges, an assumption which is justified in the frame of a mechanism of stochastic exchanges of single nucleons. It is well known that at low energy losses the results of this procedure are in rather good agreement with the number of exchanges predicted by theoretical calculations. However, with increasing TKEL, there is a growing discrepancy, as the

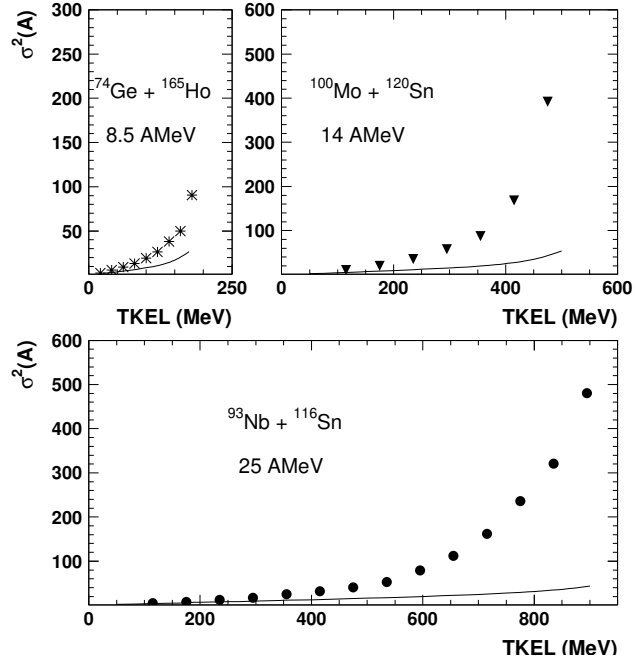


Fig. 19. Comparison of the experimental mass variances (symbols) with those calculated with the Nucleon Exchange Model (lines) for the systems $^{74}\text{Ge} + ^{165}\text{Ho}$ at 8.5 A MeV [39] (asterisks), $^{100}\text{Mo} + ^{120}\text{Sn}$ at 14.1 A MeV (triangles) [9] and $^{93}\text{Nb} + ^{116}\text{Sn}$ at 25 A MeV (circles).

mass variances tend to increase more rapidly than the theoretically calculated number of exchanges. For example, in the system $^{74}\text{Ge} + ^{165}\text{Ho}$ at 8.5 A MeV [39], already at TKEL= 100 – 150 MeV the experimental mass variances become about 2–3 times larger than predicted by NEM. In our systems, where much larger amounts of energy are dissipated, the discrepancy between experimental and calculated mass variances becomes dramatic, as it amounts to about a factor of 5 at the highest TKEL values where η_{exp} attains values of about 10. The experimental variances in comparison with NEM calculations for these three systems are shown in fig. 19.

Using the mass variances calculated in the model would give values of η_{exp} in a meaningful range, but the discrepancy with the experimental mass variances is huge and remains to be understood. One might try to explain the discrepancy by assuming that the flow directions of successively exchanged nucleons are to some extent correlated, or even that clusters of nucleons (instead of single nucleons) are transferred in a single exchange process. In this latter extreme case, one should divide the mass variance by the average mass μ of the exchanged cluster, σ_A^2/μ , in order to have an estimator of the number of elementary exchange steps. However, it seems difficult to accept values as large as $\mu = 4\text{--}5$ amu, which are needed at the highest TKEL.

In conclusion, remaining in the frame of an exchange picture it seems difficult to find a way to bring the high values of the experimental quantity η_{exp} down into a reasonable range, where it can be interpreted as a good estimator

of the excitation energy asymmetry in an elementary exchange process, η . Recalling that, conceptually, eq. 5 is worked out in the frame of a one-body exchange picture (and it loses meaning outside of that frame), this failure casts doubts on the validity (or the relevance) of such an exchange picture for describing the dissipation mechanism at these higher bombarding energies.

In any case, one should keep in mind that also other mechanisms, like fluctuations in the neck rupture, may contribute in a nonnegligible way to the excitation energy sharing and to the width broadening of the experimental mass distributions.

4.3 Angular momentum sharing and light charged particles

The experimental data on light charged particles presented in sect.3.2 show evidence for a correlation with the number of net transferred nucleons, similar to that of the total evaporation from the heavy fragments.

The multiplicity of light charged particles is an increasing function of the excitation energy of the emitting nucleus. However, due to the limited solid angle covered in the present experiment by the detector array “Le Mur”, the absolute values of the light charged particle multiplicities are affected by uncertainties larger than those associated with their ratios. Thus our analysis has been focused on the ratio between the average multiplicities of Hydrogen and Helium particles, $\langle M_H \rangle / \langle M_{He} \rangle$, emitted from the detected PLF [35].

The experimental data for particles emitted by the PLF in the direct (full circles) and reverse (full squares) collision of the system $^{93}\text{Nb} + ^{116}\text{Sn}$ at 25 AMeV are presented in fig. 20a for exit channels without net mass transfer. In agreement with the results on the average excitation energy partition presented in sect.4.1 (see also fig. 13), an equal division of the total excitation energy (estimated by TKEL) has been assumed, although the arguments that follow are rather insensitive to this hypothesis. The two sets of experimental data are very similar, possibly because of a weak dependence of the multiplicities of light charged particles on the mass of the emitting nucleus in this mass region.

On the same figure, the results of evaporation calculations with the statistical code GEMINI³ are shown by the open symbols for a ^{116}Sn nucleus in case of zero spin and large spin. In this latter case, the calculations show also the additional effect of a prolate deformation (with a representative axis ratio of 1.6), which for large spins may be more appropriate than a spherical shape. The ratio between Hydrogen and Helium particles appears to be sensitive to the angular momentum of the evaporating nucleus, with large angular momenta (and consequent deformation) favoring the emission of the more massive Helium

³ The latest version (August 2000) of the code has been used, with Hauser-Feshbach formalism for light particles up to Li ($Z_{\text{imf_min}}=4$), including the ground-unstable particles ^5He and ^5Li (exotic_index=2), and transmission coefficients from the incoming wave boundary condition model (tL_iwbc=.true.)

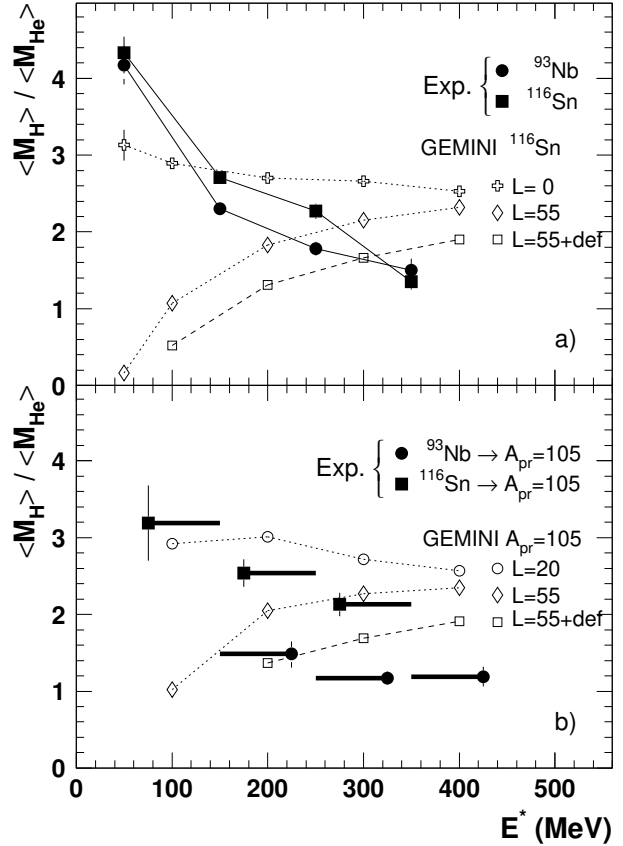


Fig. 20. a): Ratio of the experimental average multiplicities of Hydrogens and Helium particles, $\langle M_H \rangle / \langle M_{He} \rangle$, emitted by the PLF in exit channels without net mass transfer. The full circles (squares) refer to PLF from the direct (reverse) collision $^{93}\text{Nb} + ^{116}\text{Sn}$ at 25 AMeV and are plotted as a function of the excitation energy estimated from the data (see sect. 4.3 in the text). For comparison also the results of Gemini calculations for two spin values of an emitting spherical ^{116}Sn -source are shown. In case of high spin, the calculations were done also for a prolate deformed source, with an axis ratio of 1.6. b): Same presentation as in part a) except that the experimental data refer to events leading to a symmetric mass division in the exit channel and the calculations to a ^{105}Pd -source.

particles with respect to the lighter Hydrogens. Thus, the experimental rapid drop of $\langle M_H \rangle / \langle M_{He} \rangle$ with increasing E^* can be ascribed to the rise of the average angular momentum of the emitting nucleus. Indeed, the fraction of orbital angular momentum transferred into spin of the colliding nuclei is small in peripheral collisions and increases when going to more central collisions (that is to larger TKEL values) [40, 21].

Figure 20b presents the ratio of light charged particles $\langle M_H \rangle / \langle M_{He} \rangle$ emitted by the PLF for events leading to symmetric mass division in the exit channel. Again, the two sets of experimental data refer to PLF measured in the direct and reverse kinematics for the collision $^{93}\text{Nb} + ^{116}\text{Sn}$ at 25 AMeV (full circles and squares, respectively). In this case, the excitation energy E^* of the PLF has been

estimated from the measured TKEL assuming an excitation energy division in agreement with the findings on the evaporated number of nucleons (see sect.3.1.4 and fig. 10). The horizontal bars show the range of excitation energies spanned by energy divisions between the presently adopted one and that for equal energy sharing. For comparison, GEMINI calculations for a nucleus of ^{105}Pd are also drawn.

As already explained in ref. [35], for PLF measured in the direct reaction —which therefore experienced a net mass gain of nucleons— the experimental results (circles) indicate rather low ratios $\langle M_{\text{H}} \rangle / \langle M_{\text{He}} \rangle$, thus pointing to high spin values. The opposite holds for PLF measured in the reverse reaction —hence produced by a net loss of nucleons— where larger ratios $\langle M_{\text{H}} \rangle / \langle M_{\text{He}} \rangle$ indicate lower spins of the emitters. The same conclusion would hold true also in case of different excitation energy partitions, indicated by the horizontal bars of fig. 20b. Thus, with respect to the expectations for full equilibrium, the net gain (loss) of nucleons seems to be correlated with an excess (reduction) of both excitation energy *and* angular momentum sharing.

5 Conclusions

The collision $^{93}\text{Nb} + ^{116}\text{Sn}$ at 25 AMeV has been studied in direct and reverse kinematics. The analysis of primary and secondary masses of the PLF demonstrates the existence of two distinct correlations between total evaporated mass ΔA and primary mass A in the two kinematic cases. This shows that the total evaporated mass depends on the net mass transfer between the two colliding nuclei. Also the data concerning the multiplicity of light charged particles present a similar difference between the two kinematic cases. Both experimental observations, which are independent of each other, can be interpreted in terms of a dependence of the excitation energy sharing on the net mass transfer. Moreover, the measured ratios of Hydrogen and Helium multiplicities strongly point to a correlation also of the angular momentum sharing with the net mass transfer.

An explanation of the experimental findings in the frame of a stochastic exchange picture is challenged by the persisting strength of the correlation between ΔA and A even at high TKEL. The failure to obtain from the data a meaningful estimate of the excitation energy asymmetry η in an elementary exchange process casts doubts on the validity (or the relevance) of such an exchange picture for describing the dissipation mechanism at these higher bombarding energies. Indeed, with increasing TKEL and bombarding energy, other mechanisms may become important, which cannot be described simply with the elementary process of exchanging matter across a window between the two nuclei. For example, a relevant role could be played by dynamic effects, such as formation and rupture of a neck during the collision, a mechanism which in principle might explain both the correlation of excitation energy with net mass transfer and the very large experimental widths of the mass distributions. A quantitative

estimate of such collective effects is beyond the scope of the present work and requires extensive and detailed theoretical calculations.

We wish to thank the staff of the GANIL accelerator for their successful efforts to deliver high quality Nb and Sn beams pulsed with very good time structure. We are grateful to R. Ciaranfi and M. Montecchi for their skillfulness in the development of dedicated electronic modules, and to P. Del Carmine and F. Maletta for their valuable support in the preparation of the experimental set-up. We wish to thank also R. Charity for providing us with the latest version of GEMINI and for helpful discussions.

Appendix: Monte Carlo simulations

Details of the general structure of Monte Carlo simulations were already given in sect. 2.3 of ref. [1], while the Appendix A of ref. [10] was more concerned with the 3- (and 4-)body events and the typical resolutions obtained in their reconstruction.

Briefly, a binary dissipative collision is simulated on the basis of realistic distributions for the relevant physical quantities. The Total Kinetic Energy (TKE) in the exit channel is considered as the leading variable to describe the reaction mechanism. In fact, according to theoretical models and to the usually adopted picture (see *e.g.* [41]), one expects — on average — a monotonic correlation of TKE with both interaction time τ_{int} and angular momentum ℓ_{in} in the entrance channel (TKE decreases with increasing τ_{int} and with decreasing ℓ_{in}). Therefore, first of all a realistic distribution of TKE is generated and randomly sampled.

Mean values and variances of the masses and scattering angles of the reaction products are then empirically parameterized as a function of TKE and these parametrizations are iteratively tuned until realistic correlations — similar to the experimental ones — are produced, both for TKE-mass (*diffusion-plot*) and TKE- θ_{cm} (*Wilczynski-plot*).

The value of TKE is used to estimate the total excitation energy of the system (after correcting for an average Q-value between entrance and exit channel). The total excitation energy can then be divided between the two reaction partners either equally (*equal energy sharing*) or in proportion to their masses (*equal temperature sharing*) or in agreement with the excitation energy division experimentally deduced from the total number of nucleons evaporated from the fragments.

The assumed monotonic decrease of TKE with ℓ_{in} (or equivalently with impact parameter b), allows to extract also an average correspondence between TKE and ℓ_{in} , via the relation $\int_{\text{TKE}}^{E_{\text{cm}}} (d\sigma_{\text{reac}}/dE) dE = \pi\lambda^2(\ell_{\text{gr}}^2 - \ell_{\text{in}}^2)$ where ℓ_{gr} is the grazing angular momentum corresponding to E_{cm} . From theoretical models [40,21], an estimate of the dissipated angular momentum (that is of the amount of angular momentum transferred from the orbital motion into the internal degrees of freedom of the interacting system) can be obtained. The dissipated angular momentum

can then be divided between the two reaction partners either proportionally to their moments of inertia (as expected from a more equilibrated process) or with an excess in the nucleus gaining mass (as suggested by the present experimental results).

At this point, all the primary quantities of the simulated binary dissipative collision are defined and the next step is to simulate the decay of each fragment.

It was noted [1] that, for the purpose of studying just the heavy primary fragments, the particle emission in the Monte Carlo simulations needs to be nothing more than a way of adding statistical perturbations to the primary velocity vectors. As the results were not very sensitive to the adopted multiplicity distributions or relative yields of light particles, a simple rough parametrization was then good enough and no big effort was devoted to tuning the evaporation step in a realistic way.

However, in the present work, where not only the heavy reaction products but also the light charged particles are studied, it becomes important to perform a better simulation also of the evaporation step.

For each decaying primary fragment, the dependence of the evaporation step on the initial values of excitation energy E^* , spin J and mass A of the emitter is modelled according to statistical model calculations performed with the code GEMINI [27]. However, a direct event-by-event coupling of the Monte Carlo simulation code with GEMINI results unpracticable because too time-consuming. In fact, filtered simulated data with statistics comparable or even larger than the experimental data are desirable (to keep additional statistical fluctuations in the results low), but then the required computing time becomes unaffordable. Instead, a series of GEMINI calculations has been performed for a grid of values of E^* , J and A of the emitter. The multiplicities of the various evaporated light particles and intermediate mass fragments have been accordingly parametrized. Actually, as already stated in sect.3.1.3, it is necessary to tune the IMF multiplicities predicted by GEMINI in order to better reproduce the experimental spectra of ΔA and Δ_{cm} shown in fig. 8 and 9, respectively. At each step of the decay chain, the species to be emitted is randomly chosen according to the relative importance of such multiplicities. Actually, in order to mimic the correlations among successive steps of the decay chain (which are naturally displayed by the full Gemini calculations), the random choice is further weighted so as to favor decay steps leading to daughter nuclei nearer to the so-called EAL line [42].

At the moment of the emission (that is at the exit channel barrier), each particle or intermediate mass fragment has a kinetic energy of thermal origin. In order to speed up the simulation, this energy is sampled from a distribution with a (surface) Maxwellian shape, the appropriate temperature being that in the daughter nucleus at the barrier. Of course, to obtain the asymptotic kinetic energy of the particle it is necessary to add the additional contribution due to the Coulomb repulsion.

For each fragment, the evaporation process is followed along all the decay chain until the excitation energy of

the decaying nucleus is almost completely exhausted and the γ -ray decay becomes dominant (near the threshold for particle emission).

References

1. R. J. Charity *et al.*, Z. Phys. A **341**, 53 (1991)
2. B. Lott *et al.* Phys. Rev. Lett. **68**, 3141 (1992)
3. L. Beaulieu *et al.* Phys. Rev. Lett. **77**, 462 (1996)
4. B. Borderie *et al.*, Z. Phys. A **357**, 7 (1997)
5. Y. Larochelle *et al.*, Phys. Rev. C **57**, R1027 (1998)
6. J. Lukasik *et al.*, Phys. Rev. C **55**, 1906 (1997)
7. J. Töke and W. U. Schröder, Ann. Rev. Nucl. Part. Sci. **42**, 401 (1992)
8. L. Fiore *et al.*, Phys. Rev. C **50**, 1709 (1994)
9. G. Casini *et al.*, Phys. Rev. Lett. **78**, 878 (1997)
10. A. A. Stefanini *et al.*, Z. Phys. A **351**, 167 (1995)
11. G. Casini *et al.*, Phys. Rev. Lett. **67**, 3364 (1991)
12. D. R. Benton *et al.*, Phys. Rev. C **38**, 1207 (1988)
13. M. B. Chatterije *et al.*, Phys. Rev. C **44**, R2249 (1991)
14. J. Wilczynski *et al.*, Phys. Lett. B **220**, 497 (1989)
15. J. Töke *et al.*, Phys. Rev. C **44**, 390 (1991)
16. P. Klein *et al.*, Z. Phys. A **357**, 193 (1997)
17. J. L. Wile *et al.*, Phys. Rev. C **39**, 1845 (1989)
18. R. Vandenbosch *et al.*, Phys. Rev. Lett. **52**, 1964 (1984)
19. D. Pade *et al.*, Phys. Rev. C **43**, 1288 (1991)
20. J. Randrup, Nucl. Phys. A **307**, 319 (1978);
J. Randrup, Nucl. Phys. A **327**, 490 (1979)
21. J. Randrup, Nucl. Phys. A **383**, 468 (1982)
22. T. M. Semkov *et al.*, Phys. Rev. C **37**, 169 (1988)
23. L. G. Sobotka *et al.*, Phys. Lett. B **175**, 27 (1986)
24. G. A. Petitt *et al.*, Phys. Rev. C **40**, 692 (1989)
25. K. Kwiatkowski *et al.*, Phys. Rev. C **41**, 958 (1990)
26. A. Lleres *et al.*, Phys. Rev. C **48**, 2753 (1993)
27. R. J. Charity *et al.*, Nucl. Phys. A **483**, 371 (1988);
R. J. Charity *et al.*, Nucl. Phys. A **511**, 59 (1990)
28. G. Bizard *et al.* Nucl. Instr. Methods A **244**, 483 (1986)
29. G. Casini *et al.*, Nucl. Instr. Methods A **277**, 445 (1989)
30. G. Pasquali *et al.*, Nucl. Instr. Methods A **405**, 39 (1998)
31. J. Töke *et al.*, Nucl. Instr. Methods A **288**, 406 (1990)
32. S. Gralla *et al.* Phys. Rev. Lett. **54**, 1898 (1985)
33. E. Plagnol *et al.*, Phys. Rev. C **61**, 014606 (1999)
34. G. Poggi, in *Proceedings of the 7th International Conference on Nucleus-Nucleus Collisions, Strasbourg, 2000*, (to be published)
35. G. Casini *et al.*, Phys. Rev. Lett. **83**, 2537 (1999)
36. G. Fabbri (private communication)
37. G. Fabbri, M. Colonna and M. Di Toro, Phys. Rev. C **58**, 3508 (1998)
38. S. Chattopadhyay *et al.*, Phys. Rev. C **42**, R2283 (1990)
39. R. Planeta *et al.*, Phys. Rev. C **41**, 942 (1990)
40. G. Wolschin, Nucl. Phys. A **316**, 146 (1979)
41. W.U. Schröder, J.R. Birkelund, J.R. Huizenga, K.L. Wolf and V.E. Viola, Jr., Phys. Reports **45**, 301 (1978)
42. R.J. Charity, Phys. Rev. C **58**, 1073 (1998)